

**Development and Assessment of Broadband Surface Albedo from CERES Clouds  
and Radiation Swath Data Product**

David Rutan<sup>1</sup>, Fred Rose<sup>1</sup>,  
Miguel Roman<sup>2</sup>, Natividad Manalo-Smith<sup>1</sup>  
Crystal Schaaf<sup>2</sup>, and Tom Charlock<sup>3</sup>

1. Science Systems & Applications Inc, Hampton, VA
2. Boston University, Dept of Geography/Center for Remote Sensing, Boston, MA
3. NASA Langley Research Center, Science Directorate, Hampton, VA

Revised  
JGR Atmospheres  
October 2008

## Abstract

We describe a method to determine broadband albedo globally over land viewed by the Clouds and the Earth's Radiant Energy System (CERES) scanning radiometers on board the TRMM, Terra, and Aqua satellites. This albedo is used as a surface boundary condition for a fast radiation transfer code in the Surface and Atmospheric Radiation Budget (SARB) subsystem of the CERES processing scheme. Cloudy sky surface albedo is estimated from derived clear sky values. Clear sky surface albedo is assessed by comparing CERES/SARB based surface albedo to Bi-directional Reflectance Distribution Function (BRDF) based surface albedo, supplied by the MODIS land surfaces group. The SARB method employs broadband observations at the top of atmosphere (TOA) and assumes relative spectral shape of surface albedo. The MODIS group uses higher spatial resolution observations in several shortwave window channels to retrieve spectral surface albedos, then scales up to broadband surface albedo. Comparisons over snow-free land show good agreement between the two independent products on the scale of the CERES footprint. Biases run approximately 0.005 absolute, or 0.02 relative, with SARB albedo generally lower than MODIS. We find little dependence on view geometry and slight functional dependence on aerosol optical depth. The value selected for a priori surface spectral albedo is important but not critical when retrieving broadband surface albedo with broadband TOA data. But when calculating aerosol forcing to TOA flux changes in spectral albedo shape can affect aerosol forcing, as much as would a 15% absolute change in the original broadband surface albedo.

## 1. Introduction

Clouds and the Earth's Radiant Energy System (CERES) instruments, (Wielicki et al. 1996) on NASA's Tropical Rainfall Measurement Mission (TRMM), and Earth Observing System (EOS) Terra and Aqua satellites measure broadband shortwave and longwave energy reflected and emitted at the Top of the Atmosphere (TOA) as a follow on to the NASA Earth Radiation Budget Experiment (ERBE) (Barkstrom and Smith, 1986). CERES however goes beyond ERBE with advanced data products that synthesize broadband observations with other EOS data streams. One such product is the Clouds and Radiation Swath (CRS) developed by the CERES Surface and Atmospheric Radiation Budget (SARB) working group (Charlock et al., 1997, 2006). SARB runs a fast radiation transfer calculation whose location is dictated by the CERES field of view. The TRMM satellite is in a precessing orbit of  $36^\circ$ ; it observes the tropics and mid-latitudes at varying times of day. Terra and Aqua are in sun-synchronous orbits, and so view all latitudes. These orbits and the viewing capabilities of CERES and other instruments on board enable surface albedo estimates for the entire globe and for different times of day.

Broadband surface albedo is generally defined as the ratio of shortwave solar irradiance (generally between  $\sim 0.2\mu\text{m}$  and  $4.0\mu\text{m}$ ) reflected by a surface to the irradiance impinging on that same surface. Since incoming irradiance is dependent on atmospheric state, reflected irradiance is dependent upon surface properties, and both change over time, surface albedo is then clearly a continuously varying function of atmospheric and surface conditions. Hence the accuracy of a retrieval method for broadband surface albedo

69 depends upon an accurate description of the atmosphere and the reflective properties of a  
70 surface over time. The goal of this paper is to describe methodologies developed to  
71 accomplish this task for the field of view of CERES instruments and evaluate the  
72 resulting clear sky spectral and broadband estimates against independent observations.

73  
74 The accurate determination of surface albedo on a global scale is also important because  
75 of concerns regarding anthropogenic changes to the environment and its effects on  
76 radiation balance. With the advent of NASA's Earth Observing System satellites the  
77 enhanced observations of EOS make it possible to retrieve surface albedo with more  
78 confidence; one goal, for example, is estimating the radiative forcing effect of surface  
79 albedo due to changes in land cover. Radiative forcing due to anthropogenic changes to  
80 global surface albedo is addressed in the 4<sup>th</sup> IPCC report AR4-WG1-Chapter 2.5 (Forster  
81 et al., 2007). There the authors describe radiative forcing from surface albedo (reflecting  
82 land cover changes since 1750) is generally on the order of  $-0.1\text{Wm}^{-2}$  to  $-0.2\text{Wm}^{-2}$   
83 globally. (Forster et al., 2007) This is a near balance of obviously large local changes of  
84 opposing sign. CERES has the advantage of being a broadband instrument, viewing the  
85 majority of the shortwave spectrum, thus potentially giving excellent estimates of  
86 broadband surface albedo at CERES footprint time and space scales. The CERES/SARB  
87 algorithm described and assessed in this paper supplies a surface albedo that has a  
88 nominal spatial scale of  $\sim 30\text{km}$  at the Earth's surface. In "downstream" CERES data  
89 products, a similar algorithm is run for grid box means to give global, gridded surface  
90 albedo estimates. These later CERES data products can better assess the impact of global  
91 surface albedo on radiative forcing. Here we focus on methodology and assessment of the

92 surface albedos used to run the SARB radiation transfer model on a footprint-by-footprint  
93 basis and include a section on the connection between surface albedo and aerosol forcing  
94 to the shortwave flux at the top of the atmosphere.

95  
96 In this paper we consider data from EOS Terra Flight Model 1 (FM1) and Flight Model 2  
97 (FM2) CERES instruments and the radiation transfer model used in calculating the  
98 profile of irradiance beneath CERES observations. Methodology for the other CERES  
99 instrument data streams is the same. We pay particular attention to the method of  
100 defining surface characteristics observed beneath CERES footprints. Resulting surface  
101 albedos are compared to surface observations, but these point measurements are generally  
102 inadequate for validation of surface albedos determined under the large footprints, except  
103 for unusually homogeneous sites. Subsequently we use surface albedo derived by the  
104 MODerate resolution Imaging Spectroradiometer (MODIS) instrument on board Terra to  
105 assess SARB albedos. This data product originates from narrow band channels of the  
106 MODIS instrument. The algorithm is based on establishing a theoretical BRDF every  
107 eight days (Lucht et al., 2000b, Schaaf et al., 2002) and has produced valuable new data  
108 sets that provide both spectral albedo in the MODIS channels and estimates of broadband  
109 albedo at a number of spatial and temporal scales. To assess the SARB albedo, MODIS  
110 albedos are closely matched in space and time and then integrated within the field of  
111 view of the CERES instrument where we find a close agreement between broadband  
112 surface albedo from these two nearly independent sources.

We use the most currently available, respective generations of retrievals for surface albedo from MODIS and CERES that are matched in time. The MODIS Land Team uses Terra Collection 5 MODIS radiances as its source. The SARB albedos presented are from CERES CRS Edition 2B data product, which includes inputs based on the earlier generation of Terra Collection 4 MODIS radiances. For the next few years, the analyst seeking several years of concurrent surface albedos from both MODIS and CERES would likely employ the respective generations of MODIS and CERES used here. CERES CRS albedos using Collection 5 of MODIS have not yet been released. The CRS data product used here can be overwhelming due to the CERES sampling rate. The CERES Time Interpolation Spatial Averaging (TISA) working group takes CRS footprint surface albedo and averages them over the globe into a monthly, 1x1 degree grid, at the CERES overpass times. These maps, which may be more convenient than footprint data, depending on one's application, are found at the CERES/ARM Validation Experiment (CAVE) home page. (<http://www-cave.larc.nasa.gov/cave/fsw-sfcalb/>)

## 2. Clouds and the Earth's Radiant Energy System (CERES)

### *2a. CERES Instruments*

CERES instruments measure broadband radiance in three channels, shortwave (SW) reflected (mostly from 0.2 $\mu$ m to 4.0 $\mu$ m), "total broadband" (mostly 0.2 $\mu$ m to 100.0 $\mu$ m), and in the window range of ~8.0 $\mu$ m to 12.0 $\mu$ m. Longwave (LW) emitted radiation (mostly 4.0 $\mu$ m to 100.0 $\mu$ m) is inferred as the difference between the total and SW

channels. CERES Pre-Flight Model (PFM) operated for 8 months on board the TRMM satellite in 1998. Four other CERES instruments are currently on board EOS satellites, FM1 and FM2 onboard Terra, and on Aqua, Flight Models 3 and 4 (FM3 & FM4). The data rate of the CERES instruments is 100 footprints per second. Spatially the footprint size is variable depending on satellite altitude and instrument view angle. The shape of the CERES aperture and the response of the instrument in terms of energy detected, assuming a 95% response, convolve to an approximate 31km x 30km area at the surface of the Earth for a nadir view for the Terra footprint (Table 4.4-1 Green & Wielicki 1997). In this paper we utilize CERES Terra FM1 & FM2 observations in crosstrack mode.

Because direct measurements of irradiance upwelling to a satellite can represent the ERB accurately at only very coarse time and space scales (Smith and Green, 1981), it is preferable to scan for radiance and infer irradiance by applying scene-dependent, empirically-based statistical models (Suttles et al., 1988). CERES surpasses ERBE in this regard, both by inferring the scene from high resolution MODIS data (Minnis et al., 1995) and by applying fairly robust angular distribution models (ADMs) (Loeb et al., 2005) founded on the complex CERES rotating azimuth plane scan (RAPS) mode to establish BRDF on the scale of ~30 km broadband footprints; no other EOS instrument can employ RAPS to buttress the products of its routine cross-track scan. The error due to this inversion cannot be known for any single CERES footprint but it can be estimated for groups of footprints (Loeb et al., 2005, Loeb et al., 2007). Its effect however will be inherent in our derivation of surface albedo. After computing aggregate estimates of root mean square error as a function of scene type, Loeb et al. (2007) gives the rough estimate

of a TOA SW error due to inversion using ADMs of approximately 5% due to surface scene type. This estimate will be used later in a sensitivity table to analyze its effect on our estimate of broadband surface albedo. Land surface albedo is inferred from a cloud screened set of these measurements and the radiative transfer code described in the next section; the code is comparable to those used in some Global Climate Models (GCMs). The CERES derived land albedo presented here constitutes a surface boundary condition for climate models that is consistent with the ERB observations that are often used to validate the climate models at TOA.

## *2b. CERES – Surface & Atmospheric Radiation Budget (SARB)*

Within the CERES science team SARB group is tasked with calculating vertical profiles of heating rates, globally, and continuously beneath CERES footprint observations of TOA fluxes. (Charlock et al., 1997, Charlock et al., 2006) This is accomplished using a fast radiation transfer code originally developed by Qiang Fu and Kuo-Nan Liou (Fu and Liou, 1993) and subsequently modified by the SARB team. (Kato et al., 2005, Rose and Charlock, 2002); hereafter referred to as Langley Fu & Liou 2005 or (LFL05). The baseline data product for the SARB subsystem is the Clouds and Radiative Swath (CRS). Each CRS file contains one hour of CERES footprint data and includes CERES TOA observed radiances and fluxes and an analyses of those MODIS pixels collocated within the larger CERES footprint, which supply cloud properties inside the footprint. Along with CERES TOA fluxes and cloud analyses, CRS files include column fluxes at five atmospheric pressure levels, (Surface, 500hPa, 200hPa, 70hPa, and TOA) These fluxes



are a subset of the radiation transfer calculations, which are executed at higher vertical resolutions. A key input for SW calculations is spectral surface albedo under all sky conditions and for any location on the globe.

## *2c. SARB - Radiation Transfer Model and Model Input*

The SW portion of the LFL05 model is a delta-two stream radiation transfer code with fifteen spectral bands from 0.175 $\mu$ m to 4.0 $\mu$ m. Cloud optical properties within the CERES field of view are defined in a separate CERES data product, the Single Satellite Flux (SSF) product. In the SSF, MODIS imager pixels are collocated within the larger CERES footprint and weighted by the energy distribution of the CERES instrument. From these MODIS values, cloud properties, including cloud fraction (Minnis et al., 1995, 2003, 2004) are derived and used as input for the radiation transfer model. The only cloud product used in this paper is the cloud mask. Aerosol optical depths are input from MODIS (MOD08D3) product (Remer et al., 2005). When lacking the instantaneous MOD08D3 product in a CERES footprint, the first alternate is the daily, gridded MOD04, and the second is the Model for Atmospheric Transport and CHemistry (MATCH) (Collins et al., 2001), supplied courtesy of Dr. David Fillmore at NCAR, Boulder, CO. MATCH is a global aerosol model that assimilates MODIS retrievals of AOD. The MATCH model is also used to define aerosol constituents (using Optical Properties of Aerosol and Clouds, OPAC) optical properties from Hess et al., 1998, and an update to Tegen and Lacis, 1996, desert dust properties supplied courtesy of Dr. Andrew Lacis of GISS, and places aerosols throughout the vertical atmospheric column. Pressure,

temperature, and water vapor profiles are specified from GEOS-4.0 (Bloom et al., 2005), a 1-degree gridded reanalysis data product from Goddard Modeling Assimilation Office. Ozone comes from the National Center for Environmental Prediction, Stratospheric Monitoring Group Ozone Blended Analysis (SMOBA) product (Yang et al., 2000). The radiation transfer model, LFL05, is typically run for CERES footprints in which MODIS cloud properties have been derived (~2 million per day) using up to 36 atmospheric levels.

### 3. Determination of Surface Albedo

#### *3a. Estimating Broadband Surface Albedo From CERES Observations.*

As described above LFL05 currently models 15 spectral intervals (shown in Figure 1) between 0.17 $\mu$ m and 4.0 $\mu$ m in the shortwave spectrum. For each daytime CERES observation where LFL05 is run, both a surface scene dependent albedo spectral shape and an initial estimate of broadband surface albedo are required for the broader SARB operation. We now describe how these are retrieved for clear CERES footprints. To determine these values the code uses a logic sequence based on scene type determined by MODIS imager pixels collocated within the larger CERES footprint and a fixed 1/6-degree equal angle resolution global surface scene type map discussed below. After scene type is determined the algorithm utilizes look-up tables (LUT), based on radiation transfer models, to estimate an initial broadband albedo  $\alpha_{clr}$  that is consistent with the observed broadband albedo at TOA. The full LFL05 radiative transfer code is not run at

the footprint scale for this first step. This initial estimate is similar to previous methodologies for determining surface albedo (Gupta et al., 2001, Pinker & Lazlo, 1992, Rutan et al., 2006). For land, snow and ice surfaces under clear skies, the LUT is based on a parameterization of LFL05 itself. Model dependencies are shown in Equation 1.

$$\alpha_{clr} = LUT\{\alpha_{TOA}, \mu, \tau_{aod}, \omega_{aod}, T_{aod}, pw, P_{sfc}, O_3, T_{sfc}\} \dots \dots \dots Eq.1$$

Inputs to the LUT include CERES observed TOA albedo ( $\alpha_{TOA}$ ), cosine solar zenith angle  $\mu$ , aerosol optical depth  $\tau_{aod}$ , one minus aerosol single scatter albedo ( $\omega_{aod}$ ), aerosol type  $T_{aod}$ , column precipitable water (pw), surface pressure ( $P_{sfc}$ ), ozone ( $O_3$ ), and a coarse initial spectral shape parameter,  $T_{sfc}$  defined as  $\ln(A_{vis}/A_{nir})$  where  $A_{vis}$  and  $A_{nir}$  are bands 11 (0.5um to 0.7um) and 12 (0.7um to 1.3um) as shown in Figure 1 and whose determination is based on observed scene types as described in section 3b.

Equation 1 describes a LUT that is required to determine clear sky surface albedo globally under a broad range of meteorological conditions from high altitude, dry regimes such as the Antarctic plateau to moist tropical forests to bright deserts. To give an idea of the impact on the LUT to most inputs a simple sensitivity study is shown in Tables 1 and 2. There we chose a base state atmosphere shown in the top row and fixed cosine solar zenith angle of 0.5 for all runs. Next each of the remaining seven input variables are modified lower, then higher, one at a time holding the other base state variables to their original values. Table 1 shows that for most vegetated scenes the LUT is most sensitive to aerosol optical depth, precipitable water and TOA albedo. For brighter scenes, Table 2

shows the LUT is more sensitive to precipitable water, TOA albedo, and aerosol single scatter albedo.

LUT Model Sensitivity to Input Variables Base state atmosphere along with $\cos(\text{SZA}) = 0.5$ gives surface albedo $\alpha_{\text{clr}}=0.177$													
	PW		$\text{O}_3$		$\tau_{\text{aod}}$		$\text{Ln}(\text{Vis/NIR})$		$P_{\text{sfc}}$		$\omega_{\text{aod}}$		$\alpha_{\text{TOA}}$
Base State	1 cm		350 dbu		.15		0		950 mb		0.025		0.2
$\Delta$ Input	.5	3.0	300	400	.05	.35	-1	1	1000	900	0.01	0.05	.195 .205
Surface $\alpha_{\text{clr}}$	.170	.193	.175	.179	.194	.147	.180	.175	.174	.180	.177	.177	.170 .185
Range $\alpha_{\text{clr}}$	0.023		0.004		-0.047		-0.005		0.006		-0.000		0.015

Table 1. Surface albedo LUT model sensitivity to various input with initial TOA albedo typical of land scenes.

LUT Model Sensitivity to Input Variables Base state atmosphere along with $\cos(\text{SZA}) = 0.5$ gives surface albedo $\alpha_{\text{clr}}=0.754$													
	PW		$\text{O}_3$		$\tau_{\text{aod}}$		$\text{Ln}(\text{Vis/NIR})$		$P_{\text{sfc}}$		$\omega_{\text{aod}}$		$\alpha_{\text{TOA}}$
Base State	0.8 cm		350 dbu		.15		0		950 mb		0.025		0.6
$\Delta$ Input	.1	1.5	300	400	.05	.35	-1	1	1000	900	0.01	0.05	.585 .615
Surface $\alpha_{\text{clr}}$	.692	.782	.749	.759	.756	.751	.755	.753	.756	.752	.752	.765	.733 .775
Range $\alpha_{\text{clr}}$	0.091		0.010		-0.005		-0.002		-0.004		0.013		0.042

Table 2. Surface albedo LUT model sensitivity to various input parameters with bright initial TOA albedo typical of snow scenes.

The surface albedo of water (free of sea ice) is not retrieved using Equation 1. Instead it is specified from a LUT based on the Coupled Ocean Atmosphere Radiation Transfer (COART) (Z. Jin et al., 2004). This LUT has inputs of solar zenith angle, wind speed, aerosol optical depth and chlorophyll concentration. Solar zenith angle comes from CERES ephemeris data and aerosol optical depth and wind speed are available from the same products described for SARB radiation transfer described briefly above in section

2c. Global chlorophyll data products were not available when CERES CRS Edition 2B was begun and so chlorophyll is set to a constant of  $0.1\text{mg/m}^3$ .

### *3b. Estimating Albedo Spectral Shape for 15 LFL05 SW Bands*

We now address the derivation of albedo spectral shape across the required 15 LFL05 SW bands as shown in Figure 1. Because global data sets of spectral albedos were not available in the time for the full stream of CERES processing, albedo spectral shape was estimated by another route. For snow and sea ice scenes, a LUT based on a specialized

International Geosphere Biosphere Programme Global Land Cover types.	
Source of Spectral Albedo Curve CERES/SARB	
Scene Type	Spectral Curve Source
1. Evergreen Needleleaf Forest	Briegleb et al. (1985)
2. Evergreen Broadleaf Forest	Briegleb et al. (1985)(1)
3. Deciduous Needleleaf Forest	Briegleb et al. (1985)
4. Deciduous Broadleaf Forest	Briegleb et al. (1985)(3)
5. Mixed Deciduous Forest	Briegleb et al. (1985)
6. Closed Shrubland	Briegleb et al. (1985)
7. Open Shrubland	Pinker & Karnieli (1995)
8. Woody Savanna	Briegleb et al. (1985)
9. Savanna	CARE Experiment (1998) Zhou et al. 2001
10. Grassland	CARE Experiment (1998) Zhou et al. 2001
11. Permanent Wetland	Briegleb & Ramanathan (1982)
12. Cropland	CARE Experiment (1998) Zhou et al. 2001
13. Urban	Briegleb et al. (1985)(18)
14. Crop/Natural Vegetation Mosaic	CARE Experiment (1998) Zhou et al. 2001
15. Permanent Snow/Ice	Z. Jin (1994)
16. Barren/Desert	Pinker & Karnieli (1995)
17. Water Bodies	Z. Jin et al. (2004)
18. Tundra	Briegleb et al. (1985)
19. Fresh Snow	Z. Jin et al. (1994)
20. Sea Ice	Z. Jin et al. (1994)

Table 3. International Geosphere Biosphere Project (IGBP) scene types and source of albedo spectral shape.

COART model with surface snow grains (Z. Jin et al, 1994) gives albedo spectral shape. Both the CERES cloud algorithm and daily microwave maps from NSIDC and NOAA identify snow and ice. For non-snow land scenes the SARB algorithm depends upon associating predefined spectral albedos to a global surface scene type map developed from the 1km resolution map International Geosphere Biosphere Programme (IGBP) scene types (Belward, & Loveland, 1996) available from the United States Geological Survey (USGS) web site. We add an 18th type, “Tundra”, to distinguish high altitude and high latitude desert scene types identified as barren by the IGBP map. This is accomplished by folding in the Global Ecosystem Map, also from USGS (Olson et al., 1994a.) Where IGBP identifies “barren” and the Olson map identifies “tundra” we change the IGBP type to “tundra”.

To create the operational surface scene type map, we decrease the spatial resolution of the USGS IGBP map in the following manner. Each 1km IGBP type is assigned a spectral albedo from the literature or field experiments as listed in Table 3. These spectral albedos readily supply a simple fixed broadband albedo for the 18 IGBP scene types. The 1km broadband surface albedos are integrated over 10-minute (1/6 degree) equal angle grid boxes. The resulting average is compared to the list of 18 scene type based values and the closest matching IGBP type yields the albedo spectral shape that will represent that particular 10' grid box. An alternative might be to simply histogram IGBP types within each 10-minute box; but with such a method the integrated energy of the scene is potentially lost; and as we are less concerned with actual vegetation type and more

concerned with approximating the amount of radiation reflected within a given 10' box,  
we use the former method.

A further intricacy arises in the selection of albedo spectral shape because of the convention for placement of IGBP scene types within CERES footprints. The CERES data stream allows for up to eight surface types to be defined in any footprint. Two arrays define the scene and percentage of each scene within the footprint. We use the first array to act as a pointer to each scene's associated albedo spectral shape and the second array supplies weights for averaging the albedo spectral shapes within the footprint. These two arrays then supply a first estimate of an albedo spectral shape,  $\alpha_{fp}(v)$ , shown in Equation 2 where  $v$  represents the 15 spectral intervals of the LFL05 SW radiation transfer code (see figure 1) and  $w_i$  are normalized weights based on the percentage of each IGBP scene type found in any CERES footprint. Integrating this albedo spectral shape gives a broadband albedo  $A_{fp}$  flag. Note the IGBP based albedo spectral shapes do not vary over time, except for snow and ice, and so variability in the CERES IGBP vector, and subsequently our albedo spectral shape, is based purely on geography.

$$\alpha_{fp}(v) = \sum_{i=1}^{n-scenes} \alpha_i(v) w_i \dots \dots \dots Eq.2$$

We now have estimates for the CERES footprint of observed surface broadband albedo from the LUT,  $\alpha_{clr}$ , and albedo spectral shape from the IGBP map  $\alpha_{fp}(v)$ ; the next step is to reconcile the two. This is done simply by multiplying the ratio of  $\alpha_{clr}$  to  $A_{fp}$  times the albedo spectral shape  $\alpha_{fp}(v)$  as shown in Equation 3.

$$\alpha_{init}(v) = \alpha_{fp}(v) * \left(\frac{\alpha_{clr}}{A_{fp}}\right) \dots \dots \dots Eq.3$$

$\alpha_{init}$  is then the initial spectral albedo input as the surface boundary condition for running LFL05 in CERES/SARB processing for clear sky footprints. The retrieved broadband surface albedo is the ratio of the upwelling and downwelling fluxes at the surface, as computed by LFL05.

Initial broadband surface albedo for footprints viewing land surfaces where CERES has identified clouds is specified in a different manner. Derivation of an albedo spectral shape is identical to that for clear sky. However there is no instantaneous retrieval of a broadband cloudy sky land surface albedo. Instead a “history” map of albedo is created by pre-processing one month of CERES data at a time. Using the LUT in Equation 1 all clear sky footprints for a month are examined in advance and the minimum clear sky albedos are saved on a 1/6-degree equal angle resolution grid. If a grid box is cloudy for the entire month a historical value is retained or the clear sky albedo is based solely on assumed surface vegetation type. To utilize these history map values for cloudy sky footprints we require a method to “move” the broadband albedo from the solar zenith angle at which they were observed to the “diffuse” solar zenith angle (53° the Gaussian quadrature point at which the 2-stream is solved) which is used for all cloudy sky calculations in SARB processing. To accomplish this we chose the diurnal model described in Briegleb et al. (1986) shown in Equation 4. It assumes a semi-infinite canopy with randomly angled leaves for each vegetation type. Each scene type is assigned a “D” value which defines the amount by which albedo will change as a



function of changing solar zenith angle. D-values are determined from the same source as the spectral albedo for each IGBP scene type.

$$a(\mu_1) = a(\mu_0) \frac{(1 + D)}{(1 + 2D\mu_1)} \dots\dots \text{Eq.4}$$

We do not attempt to validate cloudy sky albedos in this paper. Though the limitations of this model have been elucidated (see Wang et al., 2007), due to restrictions on altering CERES climate data products, methodology once established is not changed unless new data product “Editions” are released.

#### 4. The Impacts of Aerosols and Albedo Spectral Shape on TOA SW Aerosol Forcing

How important is the assumption for albedo spectral shape of surface reflection when retrieving broadband surface albedo with observations of broadband TOA flux such as CERES? In contrast to the MODIS technique, which uses satellite spectral radiances and a model to explicitly determine spectral reflection at the surface - and then follows with an expression for broadband surface albedo, the CERES method is simple. Calculations in this section show that for typical land surfaces, the retrieval of broadband surface albedo with broadband TOA albedo as an input parameter is fairly insensitive to the assumed albedo spectral shape of surface reflection; this provides some confidence in the CERES method. It will also be apparent that CERES and MODIS products for surface albedo hinge on the fidelity of their assumptions for aerosols, both of which rely on the MODIS aerosol retrievals of Remer et al., (2005). And while factors like broadband aerosol forcing at TOA are strongly influenced by the broadband surface albedo (i.e.,

Betts et al., 2007), the spectral shape of surface albedo can also have a secondary, but significant impact on broadband aerosol forcing.

To analyze this effect we chose three distinct spectral shapes, one for a flat spectral albedo, one for a Mixed Forest scene and one for a Barren Desert scene. The Mixed Forest and Desert shapes are shown in Figure 1. LFL05 calculations with these shapes yield a broadband surface albedo of 0.3 for a mid-latitude summer atmosphere and  $\mu=0.5$ . Upwelling SW fluxes at TOA from LFL05 are shown in Figure 2. These runs are based on three spectral shapes (Mixed Forest, Barren Desert, and spectrally flat), different values for integrated broadband surface albedo (0.1, 0.2, 0.3) and aerosol optical depths (0.0, 0.2) of OPAC continental aerosol. At the TOA we find the first order effect is, of course, the increase in broadband surface albedo. The lower triplet of lines for aerosol free conditions are nearly coincident; here a retrieval of broadband surface albedo with an observed broadband flux at TOA is almost insensitive to the assumption for spectral shape. The second order effect is the change in AOD, which, regardless of spectral shape for surface reflection, increases the TOA SW flux very linearly with broadband surface albedo. The dashed line in Figure 2 shows that for a given value of observed SW at TOA, an error of 0.2 in the specification of AOD would yield an error of 0.04 in the retrieved broadband surface albedo.

The effect of albedo spectral shape is small but not negligible, and is larger when aerosol is included in the calculation. In general, if one fixes albedo spectral shape and decreases the broadband albedo, the effect will be to increase the aerosol forcing to TOA SW flux.

This is shown in Table 4 where we have used our pre-determined spectral shape for Mixed Forest. At a solar zenith angle of  $60^\circ$ , a change in broadband albedo from 0.3 to 0.2 results in a change in aerosol forcing at TOA of over  $3 \text{ Wm}^{-2}$ . Hence, 33% reduction in broadband surface albedo (0.3 to 0.2) is compensated by an approximately 28% increase in TOA aerosol forcing to SW flux ( $11.9 \text{ Wm}^{-2}$  to  $15.2 \text{ Wm}^{-2}$ ).

Aerosol Forcing to TOA SW; Fixed spectral Shape; Decrease Pristine Broadband Albedo			
$\alpha_{\text{sfc}}$	SW Up TOA (Clear Sky: AOD=0.2)	SW Up TOA (Pristine: AOD=0.0)	Aerosol Forcing (Clear-Pristine)
0.3	$189.4 \text{ Wm}^{-2}$	$177.5 \text{ Wm}^{-2}$	$11.9 \text{ Wm}^{-2}$
0.2	$148.8 \text{ Wm}^{-2}$	$133.7 \text{ Wm}^{-2}$	$15.2 \text{ Wm}^{-2}$

Table 4. Effect of broadband surface albedo on aerosol forcing to SW flux up at TOA.

In Table 5, one finds that changing albedo spectral shape but keeping broadband albedo fixed, results in a change in aerosol forcing to TOA SW that is smaller,  $1.4 \text{ Wm}^{-2}$ . Although this is only half the change to aerosol forcing of that effected by the broadband albedo change of 0.1 (0.2 versus 0.3) in Table 4, it remains notable.

Aerosol Forcing to TOA SW; Different Spectral Shapes; Fixed Broadband Albedo (0.3)			
Spectral Shape	SW Up TOA (Clear Sky: AOD=0.2)	SW Up TOA (Pristine: AOD=0.0)	Aerosol Forcing (Clear-Pristine)
Mixed Forest	$189.4 \text{ Wm}^{-2}$	$177.5 \text{ Wm}^{-2}$	$11.9 \text{ Wm}^{-2}$
Desert	$187.6 \text{ Wm}^{-2}$	$177.1 \text{ Wm}^{-2}$	$10.5 \text{ Wm}^{-2}$

Table 5. Effect of spectral surface albedo on aerosol forcing to SW flux up at TOA.

A final way to consider the effect of albedo spectral shape on TOA aerosol forcing is to look at the spectral forcing at the TOA as a function of aerosol type. Figure 3 does this by

showing the aerosol forcing to TOA albedo spectrally for two different aerosol types with fixed aerosol optical depth of 0.2. Again the mixed forest spectral shape (small reflection in the visible but sharply larger in the near infrared) is used in the radiation transfer calculation and spectral forcing in the LFL05 bands is shown for a continental aerosol (solid circles) and 2 $\mu$ m dust particles (open circles). Though total broadband aerosol forcing is approximately the same, spectrally the effect is quite different for the two aerosol types. The continental aerosol particles are small and have most of their impact in shorter wavelengths.

## 5. Assessment of CRS Surface Albedo

Y. Jin et al. (2003) and others have pointed out that validation and assessment of satellite based surface albedos is in essence a scaling problem. In their paper validating MODIS BRDF based surface albedo they compared their results against a number of various sources including observations from 10m towers at several locations around the United States and scaling up 30m LANDSAT data to the 1km MODIS pixels. They used a minute-by-minute time series of observed downwelling SW at the surface (Long and Ackerman, 2000) to exclude surface albedos measurements made under cloudy conditions from their comparison. MODIS gives distinct surface albedo products for "white sky" (isotropic illumination) and "black sky" (clear sky) conditions. By weighting MODIS black/white sky albedos by observed direct/diffuse incoming SW flux at the surface, Y. Jin et al. (2003) were able to match 10 meter tower albedo observations to within an absolute accuracy of  $\sim 0.02$  albedo units for most months of the year.

#### 5a. Comparison of CRS Albedo to Ground Observations

For the assessment of our derived clear sky albedos we have selected a number of regions where CERES data is routinely subset for validation purposes. Chosen are 25 locations scattered about the globe based on both their scene type and availability of surface observed albedo. All comparison locations are shown in Figure 8. The sites that include ground observations of albedo include the Department of Energy's Atmospheric Radiation Program (ARM) Southern Great Plains sites, NOAA's Global Monitoring Division (GMD) Surface Radiation (SURFRAD) (Augustine et al., 2000) and several Baseline Surface Radiation Network (BSRN) project (Ohmura et al., 1998), all of which adhere to the strict observational standards set by the BSRN project guidelines.

The assessment of CRS surface albedo with ground measurements is even more problematic than the MODIS albedos because of the enormous footprint size (Figure 4). Most surface observation sites are fenced, often a 10-meter tower viewing only a patch of grass that is surrounded by a different ecosystem (i.e., land grazed by cattle or used to grow crops). This incompatibility was seen in Roesch et al. (2004) when they compared MODIS to surface observations. This is confirmed in Figure 5 where CRS data and the MODIS 5km pixel closest to a surface site are compared to a number of surface observed albedos from 14 locations within our set of validation sites where albedo is observed at the surface. Because most of the spatial inhomogeneities that influence surface reflection over land are generally constant, it is then not possible to "trade space and time" as was successfully done for ocean albedo (Z. Jin et al., 2005) during the CLAMS campaign

(Smith et al., 2005). In contrast to the MODIS validation of Y. Jin et al. (2003), the surface albedos of CRS and MODIS (described in the next section) in Figure 5 are investigated at the footprint scale of CERES; ground measurements of the downwelling direct/diffuse ratio are not used to adjust the satellite-retrieved albedo; and ground measurements are not used to screen for cloud effects.

For all four months considered CERES and MODIS derived albedos are on average lower than observations from, on average, -0.02 up to -0.05 percent absolute. This translates into 10% to 25% differences in albedo relative to the surface observations. The comparison might be more favorable if the view from 10m approximated the surrounding landscape on a much larger scale. But snow cover, which is often extensive, can produce sharp seasonal contrasts in surface albedo over large areas that are faithfully represented by point measurements. Figure 6 shows a time series over five years comparing observed albedo and CRS surface albedo at the SURFRAD Fort Peck, MT site (Augustine et al., 2000). For this plot, points represent the mean albedo for a month, retrieved or observed, where that monthly mean is calculated solely at the time of the CERES observation. The Terra overpass is typically at about 1030 LST, so these are not true diurnal monthly mean values. In Figure 6 we find the SARB algorithm described in the preceding sections accurately captures inter-annual variability in albedo particularly due to snow events.

472      *5b. MODIS Surface Albedo (MCD43C2)*

473

474      Our comparisons to this point have not been consistent in scale (Figure 4): The surface  
475      albedos in Figures 5 and 6 are measured (retrieved by CRS) at scale of 10m (30km). The  
476      MODIS retrievals described below and seen in Figure 5 are at a 5km scale. In this  
477      section we scale MODIS products up to the larger size of the CERES footprints (Figure  
478      7). Such a consistent footprint-to-footprint approach is recommended by the Committee  
479      on Earth Observation Satellites (CEOS) Working Group on Calibration/Validation  
480      (WGCV), Land Product Validation (LPV) albedo subgroup. (<http://lpvs.gsfc.nasa.gov/>)

481      We have chosen the MODIS data product MCD43C2 v005 to compare with surface  
482      albedo produced from the upward/downward ratio of CRS flux calculation under clear  
483      skies. MCD43C2 is a snow free gridded data product with 0.05° equal angle spatial  
484      resolution. The gridded product is described in detail by Gao et al. (2005). This  
485      resolution corresponds to an approximate 5km “pixel” size. Temporally, the MODIS  
486      Version 5 algorithm delivers empirical BRDFs from clear sky MODIS imager data every  
487      eight days using overlapping 16-day windows (Lucht et al, 2000b; Schaaf et al 2002).  
488      The MODIS BRDF/Albedo algorithm is similar to other kernel-driven schemes used to  
489      obtain anisotropy and albedo information used by the POLarization and Directionality of  
490      the Earth's Reflectances (POLDER) instrument (Hautecoeur and Leroy, 1998; Bicheron  
491      and Leroy, 2000; Maignan et al., 2004; Bacour and Bréon, 2005) satellite sensor and  
492      Meteosat Second Generation (MSG) SEVIRI instrument (van Leeuwen and Roujean,  
493      2002; Geiger et al., 2004). Coefficients modeling the isotropic, volume, and geometric-  
494      optical surface scattering of observed vegetation and surface elements are derived for

direct (“Black Sky”) and wholly diffuse (“White Sky”) radiation. These coefficients represent the 16-day window. They are re-combined to form albedo (both spectral and broadband) using Equation 5.

$$\alpha(\nu) = \alpha_{ws}(\nu) * C(\mu, \tau_{aod}, T_{aod}) + \alpha_{bs}(\nu) * (1 - C(\mu, \tau_{aod}, T_{aod})) \dots \text{Eq.5}$$

The total albedo, at the seven spectral intervals and three broad-bands indicated as  $\nu$ , is then a linear combination of the white ( $\alpha_{ws}$ ) and black ( $\alpha_{bs}$ ) sky albedos (which are derived directly from the coefficients supplied on the MCD43C2 data product) and the coefficient  $C$  which is given by a look-up-table that is a function of aerosol optical depth, aerosol type Continental (chosen for all calculations in this comparison) or Maritime, MODIS wavelength, and solar zenith angle. The look-up-table is supplied along with the data product. Spectrally, the product supplies seven narrowband visible and near infrared channels and three broadband estimates based on weighting functions described by Liang et al. (1999). These data have been validated in several publications. The accuracy of the MODIS operational albedos marked as high quality by the quality assurance flags is less than 5% relative at validation sites studied thus far and even those albedo values with low quality flags have been found to be within 10% relative of field data (Y. Jin et al., 2003, Salomon et al., 2006). To match the CERES footprints temporally with MODIS data we have restricted the CERES observations to within the 16-day period of the MCD43C2 data product and selected only two MODIS files per month. For example in January 2001 we chose MODIS files dated Jan 1 and Jan 17. The BRDFs in these files are drawn from clear sky MODIS pixels from Jan 1 through Jan 16 and Jan 17 through Feb 1 respectively, the same time periods within which we match the CERES footprints to the



MODIS data. This avoids the possibility of selecting a CERES footprint for more than one comparison. The MODIS Collection 4 AOD (the actual MOD08 retrieval is preferred but the interpolated daily average MOD04 or MATCH aerosol assimilation are more commonly used) is an important parameter in the determination of the CRS surface albedo by CERES. In contrast, the MCD43C2 v005 coefficients for a 16-day window are employed MODIS Collection 5. To achieve a footprint-by-footprint comparison (i.e., recommendation of CEOS) that is more relevant to users (note last paragraph of Introduction), we express the MODIS surface albedo from the MCD43C2 v005 coefficients with the same Collection 4 AODs used by CRS.

### *5c. Integration of MODIS into a CERES CRS Footprint Field-of-view*

Matching the MODIS data to the CERES field-of-view is necessary for an appropriate comparison of the two products. The term “footprint” refers to a CERES field-of-view (FOV) of the surface while the term “pixel” will be defined as the MCD43C2 0.05° grid box. Our methodology for matching MODIS pixels to the CERES footprint follows this path. We locate a CERES footprint center on the 0.05° MODIS grid and determine footprint length. The footprint itself is associated with a smoothly varying “point spread function” (PSF) that describes the change in detector response with respect to the location of an energy source within the footprint. This energy response changes as a function of viewing zenith angle (VZA), elongating in the forward view and compressing in the back as shown schematically in Figure 7. Hence the center of a CERES footprint (given as a latitude and longitude at the surface in all CERES data products) is the energetic center

with respect to view zenith angle (Figure 7). The length and shape of a footprint thus changes from a near circle with diameter  $\sim 30\text{km}$  at nadir view angle, to an ellipsoidal shape with length near  $200\text{km}$  at  $70^\circ$  VZA. When integrating other variables within a CERES footprint one needs to take this energy response into account giving less weight to pixels near the edge of the footprint and more weight to pixels near the center.

For the purposes of this study we assume the CERES footprint is a circle whose center is located by the CERES surface latitude/longitude with a radius of  $1/2L$  (where  $L$  is the length of the CERES footprint along the scan angle.) We approximate the energy response of the instrument as a normalized distance of  $1/L$  from this center. MODIS albedos are then integrated within the CERES footprint, weighting the MODIS regions as  $d/L$  where “ $d$ ” is the physical distance from the footprint center to the center of the MODIS pixel. At nadir viewing angles the CERES footprint will closely match with our assumption. However as VZA increases the circular shape and actual area viewed will begin to diverge. The more heterogeneous the surface is in elevation, scene type etc... the more error we might expect due to these assumptions.

In this comparison we only consider footprints free of clouds as determined in the CERES data product. CERES CRS product includes an independent cloud analysis of MODIS  $1\text{km}$  observations within each CERES footprint (Minnis et al., 1995). We only consider footprints where the CERES cloud fraction is  $0.0$ , which is to say the cloud algorithm determined all collocated MODIS  $1\text{km}$  pixels to be cloud free. At times, the MODIS BRDF albedo upon which we locate the CERES footprint is incomplete. We

interpolate the MODIS BRDF coefficients in space if the missing portion of the field is less than 20% of the footprint. Otherwise we disregard that footprint.

## 6. Results of CRS and MODIS broadband albedo comparison

### *6a. Assessment of CRS broadband surface albedo at 'land' sites*

In this section we compile results of the MODIS surface albedo integrated within CERES footprints for eight MCD43C2 data files. Chosen were the months of January, April, July, and October 2001. Figure 8 shows the locations on the globe where comparisons were made. These regions were previously designated “CERES validation regions” and are approximately 111km square regions where subsets of CERES data are extracted from formal data processing for the purpose of validating CERES algorithms. For our purposes we retain only footprints whose center is less than 25km of each surface site for each satellite overpass to limit the sample. Black filled diamonds indicate land surface sites and open diamonds are designated desert surface sites.

	Jan	Apr	Jul	Oct	All Months
CRS Mean	0.145	0.150	0.154	0.161	0.154
MODIS Mean	0.153	0.153	0.158	0.165	0.158
Absolute Bias	-0.008	-0.003	-0.003	-0.003	-0.004
Absolute RMS	0.020	0.018	0.013	0.015	
Relative Bias	-5.2%	-2.0%	-2.0%	-1.8%	-2.4%

Table 6. Monthly mean albedo differences between CRS albedo and MODIS albedo integrated within CERES Terra FM1 for land footprints for four months in 2001.

Complete results for 25 land sites for the months considered are shown in Figure 9. The majority of these sites are located in the northern hemisphere. Subsequently the number

of clear sky comparisons peak in October whereas in January, due to snow in the scenes, which has been removed, we find the least number of clear sky comparisons. Though there is some seasonal variability, overall the comparisons are quite good as measured by mean bias and RMS for each month as shown in Table 6. Bias for all months is negative with a mean of -0.004 absolute, leaving a relative bias of just -2.4% (as if CERES were "darker" than MODIS). The RMS runs from a low of 0.013 in July to 0.020 in January.

The conspicuous "tail" of low CRS albedos in April 2001 (Figure 9b) is largely due to data from a single location (north latitude 53.5, longitude 273.9) with evergreen forest to the south of Hudson Bay in eastern Canada (Figure 8). There, MODIS albedo remains stable near 0.10 while the CRS albedo varies between 0.03 and 0.13. The reasons behind the retrieved surface albedos (as low as 0.03), which is so low as to strain credibility for a large footprint over land, is instructive for the EOS user. Collection 4 AOD reported by the MODIS Atmosphere Team for this site in April 2001 are both quite high and quite variable. The algorithm used by the MODIS Land Team preferentially chooses cloud-free pixels with low AOD (less obscuration) for the retrieval of surface albedo, so MCD43C2 v005 coefficients supplied by the MODIS Land Team are generally founded on the low AOD observations in each 16-day block. While Equation 5 shows that the MODIS surface albedo explicitly depends on AOD, the day-to-day change in AOD has only a fairly small effect by apportioning the fraction of "white" and "black" sky. The dashed line in Figure 2 draws attention to the contrastingly large impact of any change in AOD on the CRS albedo. As MODIS pixels are very small, there are usually a sufficient number in a local domain for the 16-day reporting period for the MODIS surface albedo

product. Because CERES footprints are large, they are often not clear. Thus every available clear CERES footprint over land is used to retrieve a surface albedo, regardless of AOD. For the site in eastern Canada in April 2001, CRS reported 20 clear footprints with simultaneous retrievals of AOD by MODIS. The thirteen CERES CRS footprints with high AOD (mean 0.67) gave an unrealistically low mean surface albedo of 0.05; the other seven (mean AOD of 0.32) had a mean albedo of 0.11. The surface albedos from the MODIS Land Team are in this case (the tail) more realistic than those from CERES, and the source of this CERES deficiency in surface albedo appears to lie in some surprisingly high values of AOD from the MODIS aerosol product. The range of expected values from the MODIS v004 aerosol product defined by Remer et al. (2005) is  $\pm 0.05 \pm 0.15 \tau_{\text{aod}}$  when compared to surface observed aerosol from the AERONET network. Though high, it is unknown if the value of .67 lies outside this range as there is no surface observation against which to compare. However the LUT sensitivity is largest to aerosol optical depth over snow free land albedos as shown in Table 2. If the radiative transfer calculations with the MODIS surface albedos were run for the high AOD cases, they would yield TOA albedos much larger than those observed with the CERES broadband instrument; we know this because the CRS calculations (having low surface albedos) agree with CERES observations. Such a conspicuous tail of low albedo (Figure 9b) is not found to the same degree in any other month. But the CRS routine of retrieving a surface albedo value for every clear CERES footprint over land, regardless of the uncertainty for the input AOD, has yielded a product which is much more noisy than MODIS; note the results for 14 sites in Figure 5.

633 *6b. Assessment of CRS broadband surface albedo at ‘desert’ sites*

634  
635 Departing the tail of Figure 9b, we return to the domain of 25 sites for all four months. In  
636 figures 10 and 11 we show the difference between CRS and MODIS albedos as a  
637 function of AOD and precipitable water (Fig 10) and solar zenith and viewing zenith  
638 angles (Fig 11). In each case there appears little functional relationship except for the  
639 case of aerosol optical depth where differences typically increase as AOD increases.  
640 Recall that while MODIS albedos (Equation 5) assume only two aerosol types  
641 (continental or marine), the MATCH assimilation used by CERES supplies up to seven  
642 types (large dust, small dust, sulfate, marine, soot, soluble organic carbon, and insoluble  
643 organic carbon) that are used to assign the spectral single scattering albedos and  
644 asymmetry parameters. The atmospheric correction used in the CERES retrieval of  
645 surface albedo includes the effect of absorption by aerosols that are more variable than in  
646 the MODIS retrieval.

647  
648 Figure 12 and Table 7 compare surface albedos at four desert sites only. Again, this  
649 comparison is quite good both visually and in terms of absolute and relative biases, -2.1%  
650 for desert versus -2.4% for all sites. Despite the larger mean surface albedo over deserts,  
651 the homogeneous nature of the desert scenes produces values for the absolute RMS  
652 (Table 7) that are hardly larger than those for all sites (Table 6). The four desert sites  
653 (Figure 12 and Table 7) can be placed in three categories: Albedos less than 0.2 come  
654 from the SURFRAD Desert Rock, NV (DRA) site. Those between 0.2 and 0.3 are located  
655 at the BSRN, Tamanrasset, Algeria (TAM) site. Albedos greater than 0.3 come from the

	Jan	Apr	Jul	Oct	All Months
CRS Mean	0.283	0.284	0.278	0.289	0.283
MODIS Mean	0.292	0.289	0.284	0.291	0.289
Absolute Bias	-0.008	-0.006	-0.007	-0.002	-0.006
Absolute RMS	0.019	0.017	0.021	0.018	
Relative Bias	-2.7%	-2.1%	-2.5%	0.7%	-2.1%

Table 7. Monthly mean albedo differences between CRS albedo and MODIS albedo integrated within CERES Terra footprints at 4 desert locations for four months in 2001.

BSRN, Sede Boqer, Israel (SBO) site and the Saudi Solar Village (SSV) (Myers et al. 1999) site. Each of the three desert categories displays a characteristic bias: At DRA CRS albedo is consistently greater than the MODIS. At TAM, CRS albedo is consistently lower than MODIS. And at SBO and SSV the two retrievals tend to agree.

The difference of CERES and MODIS albedos in Figure 13 (the desert analog to Figure 10) again shows little relationship to precipitable water, but a stronger dependence on AOD. For the deserts however there is significantly more aerosol found (note that the x-axis scale has doubled over that shown for the land sites in Figure 10). Figure 14 shows the difference between MODIS and CRS albedos as a function of VZA and SZA. The “clumping” of footprints as a function of VZA shows that regionally there is dependence of the comparison on view zenith angle, at times approaching 1% to 2% absolute albedo. Likewise with solar zenith angle, in every season but January there appears a positive trend of the difference as SZA increases. When the desert data are broken down site by site, the majority of the solar zenith angle dependence is attributable to footprints at TAM during Apr, Jul and Oct but not Jan. The effect is exacerbated by the fact that DRA has a permanent positive bias. The reason for the dependence at TAM during Northern Hemisphere summer is at this point unknown though one possibility may be the fidelity

of the MODIS BRDF model. At these times at TAM there was very little Collection 5 aerosol available to the land surfaces group for the derivation of the BRDF.

#### *6c. Assessment of CRS albedo spectral shape*

Surface albedo input into LFL05 model is in 15 spectral bands between 0.2 $\mu$ m and 4.0 $\mu$ m. As stated above spectral shape used in SARB is solely a function of the (up to eight) spectral shapes based on the IGBP types found in the CERES footprint. CERES/SARB has compiled only 16 different IGBP types, each with a respective spectral shape, to span the globe; the coverage of snow and ice is the only seasonality. On the other hand, MODIS BRDFs and albedos are not constrained to such assumptions for albedo spectral shape, as they are retrieved using MODIS radiances from seven narrowband channels. MODIS albedo spectral shapes themselves are of course dependent on the ability of the MODIS algorithm to retrieve a representative BRDF model given available clear sky radiances retrieved over each sixteen-day period. Over snow, desert (with heavy aerosol loading) and persistently cloudy areas the MODIS BRDF can and does, revert to a default model which is noted in MCD43C2 quality parameters within the MODIS data product. So whereas we might assume that CERES has the greater potential to retrieve a quality broadband surface albedo, the MODIS instrument is capable of retrieving a better albedo spectral shape. So the question of how well do the CERES albedo spectral shapes compare to those from the MODIS data product arises? As a gross assessment of a priori spectral shape used by CRS, statistics were compiled as a function of wavelength for the resulting spectral albedos from the footprints in Figures 9 (land)



and 12 (desert). These statistics were then plotted; means (solid circles), standard deviations (vertical bars), minimums and maximums (hats), in Figures 15 (land) and 16 (desert). The color gray indicates results from MODIS, black, results from CRS. For all land surface types in Fig 15 we find a fairly good agreement in the shortwave portion of the spectrum below 1 micron in all months with some key differences. In January the 0.63 $\mu$ m channel is brighter in MODIS than in the CRS average. In fact the mean CRS value falls near the minimum MODIS value. At the important 0.86 $\mu$ m channel (band 0.69-1.30 $\mu$ m for LFL05) means and standard deviations are comparable, but minimum values of CRS are significantly lower than those of MODIS. Mean values match well in April and July, though are lower for CRS in January and October. The comparison is not as good for wavelengths greater than 1.0 micron, where for each month the CRS values underestimate those reported by the MODIS product. These wavelengths contribute to the consistently negative tendency of CRS broadband albedo (compared with MODIS) shown in Figures 9 and 12. Roughly 23% of the solar insolation at the surface is found at wavelengths above 1.0 $\mu$ m, for a climatological mid-latitude summer at a solar zenith of 60 degrees. It appears that CRS albedo spectral shapes could be improved by folding in MODIS values. Figure 16 shows the same spectral albedo comparison as Figure 15 but for four desert sites whose broadband albedo comparison is found in Figure 12. As desert scenes tend to simpler spectral shape, these comparisons match slightly better than those for the land scenes. Below 1 micron the comparison is quite good however, again for wavelengths greater than 1 micron the CERES CRS spectral shapes underestimate the mean values found at the desert sites by the MODIS albedos.

## 7. Conclusions

We have described in detail the methodology for deriving clear and cloudy sky broadband albedo and spectral shape for use, globally; by applying the radiation transfer routines used in CERES/SARB subsystem that produces the Clouds and Radiation Swatch (CRS) data product. The importance of accurately defining spectral surface albedo is justified due to the impact of the interaction of aerosols and albedo with respect to the forcing of SW flux at the top of the atmosphere. For clear sky footprints the methodology is assessed against an independent product from the higher spectral resolution MODIS instrument on board the same EOS Terra satellite. Comparisons of the CERES CRS surface albedo to surface observed albedos from radiometers mounted at 10 meters are untenable. Instead, as encouraged by the CEOS/WGCV/LPV Albedo Subgroup, we integrate MODIS BRDF based albedos into the CERES footprints and compare these integrated values against the ratio of the upward to downward fluxes as calculated by the SARB code. Matching these independent products in space and time, and weighting the MODIS according to an approximation of the energy response of the CERES instrument, shows significantly improved results over comparisons with albedo observed from instruments mounted on 10m towers as found in Figure 5. Over land sites, mean difference for all footprints compares are -0.004 absolute, or 2.4% relative to the MODIS product means. RMS also remains small from 0.015 to 0.020 depending on month. These values of RMS are approximately 10% relative to the MODIS albedo mean.

When only the more homogeneous desert footprints are considered, absolute bias remains approximately the same at -0.006. However, mean albedo and mean solar zenith angle for these latitudes also increase and the relative bias with respect to mean MODIS albedo actually drops to 2.1%. Mean RMS for the four desert months/footprints considered is approximately 0.02 or less than 10% of the MODIS mean albedo.

For both desert and land scene types, for all months, we find the difference between the two albedo products increases as aerosol optical depth increases. There was some dependence in desert scenes of the albedos on VZA of the CERES instruments as well as a slight positive slope dependence of the desert albedos on SZA. These dependencies tend to cancel in the mean. A comparison of spectral shapes, based on a gross average of all footprints for the two clear sky scene types, determined that in general the two products match better in the shorter wavelengths than for those above 1 micron.

Each large, clear CERES CRS footprints over land has its own retrieval for surface albedo. The CRS product for land surface albedo at Terra overpass appears to be reasonably accurate but rather noisy with input for AOD as a principal source of the noise. A comparison with MODIS retrievals and ground-based observations indicates CRS surface albedos tend to have a low bias. Filtering based on AOD may be the way to produce a more useful monthly CRS surface albedo. Succeeding generations of CERES data products for surface albedo may be more useful for calculation of aerosol forcing by incorporating information on spectral albedo from the MODIS Land Team.

## *Acknowledgements*

The authors would like to thank the anonymous reviewers whose close reading and suggestions led to a better-organized and stronger paper. CERES data is supplied from the NASA Langley Research Center Atmospheric Sciences Data Center. MODIS data is supplied from the NASA Goddard Distributed Active Archive Center. ARM data is made available through the U.S. Department of Energy as part of the Atmospheric Radiation Measurement Program. GMD data are made available through the NOAA's Earth System Research Laboratory/Global Monitoring Division - Radiation (G-RAD). SURFRAD data is made available through NOAA's Air Resources Laboratory/Surface Radiation Research Branch. C. Schaaf and M. Roman are supported by NASA NNX08AE94A and DOE DE-FG02-06ER64178

## 8. References

- Augustine, J. A., J. J. DeLuisi, and C. N. Long, 2000: SURFRAD-A National Surface Radiation Budget Network for Atmospheric Research, Bull. of Amer. Met. Soc. Vol. 81, No. 10, pp. 2341-2358.
- C. Bacour and F-M. Bréon, 2005: Variability of biome reflectance directional signatures as seen by POLDER. Rem. Sens. Env. 98, 80-95. doi:10.1016/j.rse.2005.06.008
- Barkstrom, B. R., and G.L. Smith, 1986: The Earth radiation budget experiment: Science and implementation, Rev. Geophys., 24, 379-390.

791 Belward, A., and T. Loveland, 1996: The DIS 1km Land Cover Data Set, GLOBAL  
792 CHANGE, The IGBP Newsletter, #27, Sep.

793 Betts, A. K., and J. H. Ball, Albedo Over the Boreal Forest, J. Geophys. Res., 102, 28901  
794 28909, 1997.

795 Betts. R. A., P. D. Fallon, K. K. Goldewijk, and N. Ramankutty, 2007: Biogeophysical  
796 effects of land use on climate: Model simulations of radiative forcing and large-scale  
797 temperature change, J. of Agr. and For. Met. 142, no. 2-4, 216-233.

798 Bicheron, P., and M. Leroy: 2000, Bidirectional reflectance distribution function  
799 signatures of major biomes observed from space. J. Geophy. Res., 105(21), 26669 –  
800 26681

801 Bowker, D.E., R.E. Davis, D.L. Myrick, K. Stacy, and W.T. Jones, 1985: Spectral  
802 Reflectances of Natural Targets for use in Remote Sensing Studies, NASA Ref. Pub.,  
803 1139.

804 Bloom, S., A. da Silva, D. Dee, M. Bosilovich, J.-D. Chern, S. Pawson, S. Schubert, M.  
805 Sienkiewicz, I. Stajner, W.-W. Tan, M.-L. Wu, 2005: Documentation and Validation  
806 of the Goddard Earth Observing System (GEOS) Data Assimilation System - Version  
807 4 . Technical Report Series on Global Modeling and Data Assimilation 104606 , 26.  
808 Document (18124 kb) <http://gmao.gsfc.nasa.gov/systems/geos4/>

809 Briegleb, B.P., P. Minnis, V. Ramanathan, and E. Harrison, 1986: Comparison of  
810 Regional Clear-Sky Albedos Inferred from Satellite Observations and Models  
811 Comparisons, J. Clim. Appl. Meteor., 25, 214-226.

812 Briegleb, B.P., and V. Ramanathan, 1982: Spectral and Diurnal Variations in Clear Sky  
813 Planetary Albedo, J. Appl. Meteor., 21, 1160-1171.

Charlock, T. P., F. G. Rose, D. A. Rutan, T. A. Alberta, D. P. Kratz, L. H. Coleman, G. L. Smith, N. M. Smith, and T. D. Bess, 1997: Clouds and the Earth's Radiant Energy System (CERES) Algorithm Theoretical Basis Document: Compute Surface and Atmospheric Fluxes (Subsystem 5). (<http://science.larc.nasa.gov/ceres/ATBD/>)

Charlock, T. P., F. G. Rose, D. A. Rutan, Z. Jin, and S. Kato, 2006: The Global Surface and Atmosphere Radiation Budget: An Assessment of Accuracy with 5 years of Calculations and Observations. Proceedings of 12th Conference on Atmospheric Radiation (AMS), 10-14 July 2006, Madison, Wisconsin.

Collins, W. D., P. J. Rasch, B. E. Eaton, B. V. Khattatov, J.-F. Lamarque, and C. S. Zender, 2001: Simulating aerosols using a chemical transport model with assimilation of satellite aerosol retrievals: Methodology for INDOEX. *J. Geophys. Res.*, 106, 7313-7336.

Dickinson, R. E., 1983: Land surface processes and climate – Surface albedo and energy balance. *Adv. in Geophys.*, 25, 305-353.

Forster, P., V. Ramaswamy, P. Artaxo, T. Berntsen, R. Betts, D.W. Fahey, J. Haywood, J. Lean, D.C. Lowe, G. Myhre, J. Nganga, R. Prinn, G. Raga, M. Schulz and R. Van Dorland, 2007: Changes in Atmospheric Constituents and in Radiative Forcing. In: *Climate Change 2007: The Physical Science Basis. Contribution of Working Group I to the Fourth Assessment Report of the Intergovernmental Panel on Climate Change* [Solomon, S., D. Qin, M. Manning, Z. Chen, M. Marquis, K.B. Averyt, M. Tignor and H.L. Miller (eds.)]. Cambridge University Press, Cambridge, United Kingdom and New York, NY, USA.

836 Fu, Q., G. Lesins, J. Higgins, T. Charlock, P. Chylek, and J. Michalsky, 1998:  
 837 Broadband water vapor absorption of solar radiation tested using ARM data.  
 838 Geophys. Res. Let., 25, 1169-1172.

839 Fu, Q., and K-N. Liou, 1993: Parameterization of the radiative properties of cirrus  
 840 clouds. J. Atmos. Sci., 50, 2008-2025.

841 Gao, F., C. B. Schaff, A. H. Strahler, A. Roesch, W. Lucht, and R. Dickinson 2005:  
 842 MODIS bi-directional reflectance distribution function and albedo Climate Modeling  
 843 Grid products and the variability of albedo for major global vegetation types, J.  
 844 Geophys. Res., 110, D01104.

845 Geiger, B., O. Samain, F. Baret, O. Hagolle, P. Bicheron, J.-L. Roujean, L.  
 846 Franchisteguy, M. Leroy, 2004: Multi-sensor data fusion for deriving bio-physical  
 847 variables in the Cyclopes project. Geoscience and Remote Sensing Symposium,  
 848 IGARSS '04. Proceedings. Vol 4, 2524- 2527

849 Green, R., B. A. Wielicki, Clouds and the Earth's Radiant Energy System (CERES)  
 850 Algorithm Theoretical Basis Document: Convolution of imager cloud properties with  
 851 CERES footprint point spread function (Subsystem 4.4).  
 852 (<http://science.larc.nasa.gov/ceres/ATBD/>)

853 Grenfell, T.C., S.G. Warren, and P.C. Mullen, 1994: Reflection of Solar Radiation By  
 854 The Antarctic Snow Surface at Ultraviolet, Visible, and Near-Infrared Wavelengths,  
 855 J. Geophys. Res., 99, 18669-18684.

856 Gupta, S. K., D. P. Kratz, P. W. Stackhouse, and A. C. Wilber, 2001: The Langley  
 857 Parameterized Shortwave Algorithm (LPSA) for Surface Radiation Budget Studies,  
 858 NASA TP 2002-211272, 31 pp.

Hautecœur, O., M. Leroy, 1998: Surface bidirectional reflectance distribution function observed at global scale by POLDER/ADEOS, *Geophys. Res. Ltrs.* 25, p. 4197-4200  
DOI: 10.1029/1998GL900111

Hess, M., P. Koepke, and I. Schult, 1998: Optical Properties of Aerosols and Clouds: The software package OPAC. *Bull. Amer. Meteor. Soc.*, 79, 831-844.

Jin, Y., C. B. Schaaf, C. E. Woodcock, F. Gao, X. Li, A. H. Strahler, W. Lucht, and S. Liang, 2003: Consistency of MODIS surface bidirectional reflectance distribution function and albedo retrievals, 2. Validation. *J. Geophys. Res.*, 108, no. D5, 4159,

Jin, Z., K. Stamnes, W. F. Weeks, and S. C. Tsau, 1994: The effects of sea ice on the solar energy budget in the atmosphere-sea ice-ocean system: A model study. *J. Geophys. Res.*, 99, 25,281-25,294.

Jin, Z., T. P. Charlock, W. L. Smith, and K. Rutledge, 2004: A parameterization of ocean surface albedo., *Geophys. Res. Lett.*, 31, L22301.

Jin, Z., T. P. Charlock, K. Rutledge, G. Cota, R. Kahn, J. Redemann, T. Zhang, D. A. Rutan, and F. Rose, 2005: Radiative transfer modeling for the CLAMS experiment. *J. Atmos. Sci.*, 62, 1053-1071.

Jin, Z., T. P. Charlock, P. Yang, S. R. Hudson, and S. G. Warren, 2008: Snow optical properties for different particle shapes with application to snow grain size retrieval and MODIS/CERES radiance simulation over Antarctic. In press for *Rem. Sens. of Env.*

Kato, S., F.G., Rose, and T.P., Charlock, 2005: Computation of Domain-Averaged Irradiance Using Satellite-Derived Cloud Properties, *J. of Atmos. Ocean. Tech.*, 22b, pp 146-164.



van Leeuwen, W. and J.-L. Roujean, 2002: Land surface albedo from the synergistic use of polar (EPS) and geo-stationary (MSG) observing systems; An assessment of physical uncertainties. *Rem. Sen. of Env.*, 81, 273-289.

Liang, S., A. H. Strahler, and C. W. Walthall, 1999: Retrieval of land surface albedo from satellite observations: A simulation study, *J. Appl. Meteorol.*, 38, 712-725.

Loeb, N. G., S. Kato, K. Loukachine, and N. Manalo-Smith, 2005: Angular distribution models for top-of-atmosphere radiative flux estimation from the Clouds and the Earth's Radiant Energy System on the Terra satellite. Part I: Methodology. *J. Atmos. Ocean. Technol.*, 22, 338-351.

Loeb, N. G., S. Kato, K. Loukachine, N. Manalo-Smith and D. R. Doelling, 2007: Angular distribution models for top-of-atmosphere radiative flux estimation from the Clouds and the Earth's Radiant Energy System on the Terra satellite. Part II Validation. *J. Atmos. Ocean. Technol.*, 22, 338-351.

Long, C. N., and T. P. Ackerman, 2000: Identification of clear skies from broadband pyranometer measurements and calculation of downwelling shortwave cloud effects. *J. Geophys. Res.*, 105, 15,609-15,626.

Lucht, W., C. B. Schaaf, and A. H. Strahler, (2000b), An algorithm for the retrieval of albedo from space using semi-empirical BRDF models, *IEEE Trans. Geosci, Remote Sens.*, 38, 977-998.

Maignan, F., F.-M., Breon, R. Lacaze, (2004). Bidirectional reflectance of Earth targets: Evaluation of analytical models using a large set of spaceborne measurements with emphasis on the hot spot. *Rem. Sens. of Env.*, 90, pp. 210-220.

Minnis, P., D. P. Kratz, J. A. Jr. Coakley, M. D. King, D. Garber, P. Heck, S. Mayor, D.  
 F. Young, and R. Arduini, 1995: Cloud Optical Property Retrieval (Subsystem 4.3).  
 "Clouds and the Earth's Radiant Energy System (CERES) Algorithm Theoretical  
 Basis Document, Volume III: Cloud Analyses and Radiance Inversions (Subsystem  
 4)", NASA RP 1376 Vol. 3, edited by CERES Science Team, December, 1995, pp.  
 135-176.

Minnis, P., D. F. Young, S. Sun-Mack, P. W. Heck, D. R. Doelling, and Q. Trepte, 2003:  
 CERES Cloud Property Retrievals from Imagers on TRMM, Terra, and Aqua, Proc.  
 SPIE 10th International Symposium on Remote Sensing, Conference on Remote  
 Sensing of Clouds and the Atmosphere VII, Barcelona, Spain, September 8-12, 37-  
 48.

Minnis, P., D. F. Young, S. Sun-Mack, Q. Z. Trepte, R. R. Brown, S. Gibson, and P.  
 Heck, 2004: Diurnal, seasonal, and interannual variations of cloud properties derived  
 for CERES from imager data. Proc. of the Thirteenth American Meteorological  
 Society Conference Satellite Oceanography and Meteorology, Norfolk, Virginia,  
 September 20-24, CD-ROM, P6.10.

Myers, D. R., S. Wilcox, M. Anderberg, S. H. Alawaji, N. M. Al Abbadi, M. Y. bin  
 Mahfoodh, 1999: Saudi Arabian solar radiation network of data for validating satellite  
 remote-sensing systems, Earth Obs. Sys. IV SPIE Vol 3750, 18-20 July, Denver CO.

Ohmura A., E. Dutton, B. Forgan, C. Frohlich, H. Gilgen, H. Hegne, A., Heimo, G.,  
 Konig-Langlo, B. McArthur, G. Muller, R. Philipona, C. Whitlock, K. Dehne, and M.  
 Wild, (1998): Baseline Surface Radiation Network (BSRN/WCRP): New precision

926 radiometry for climate change research. Bull. Amer. Meteor. Soc., 79, No. 10, 2115-  
 927 2136.

928 Olson, J.S. (1994a), Global Ecosystem framework-definitions: USGS ERSO Data Center  
 929 Internal Report, Sioux Falls, SD, 37pp.

930 Pinker, R. T., and I. Laszlo, 1992: Modeling of surface solar irradiance for satellite  
 931 applications on a global scale. J. Appl. Meteorol., 31, 195-211.

932 Pinker, R. T., and A. Karnieli, 1995: Characteristic Spectral Reflectance of A Semi-Arid  
 933 Environment, Int. J. Rem. Sens., RS100424.

934 Remer, L. A., Y. J. Kaufman, D. Tanre, S. Mattoo, D. A. Chu, J. V. Martins, R.-R. Li, C.  
 935 Ichoku, R. D. Levy, R. G. Kleidman, T. F. Eck, E. Vermote, and B. N. Holben, 2005:  
 936 The MODIS aerosol algorithm, products, and validation. J. Atmos. Sci., 62, 947-973.

937 Roesch, A., C. Schaaf, and F. Gao, 2004: Use of Moderate-Resolution Imaging  
 938 Spectroradiometer bi-directional reflectance distribution function products to enhance  
 939 simulated surface albedo, J. Geophys. Res., 109, D12105.

940 Rose, F. G., and T. P. Charlock, 2002: New Fu-Liou Code Tested with ARM Raman  
 941 Lidar and CERES in pre-CALIPSO Exercise. Extended abstract for 11th Conference  
 942 on Atmospheric Radiation (AMS), 3-7 June, Ogden, Utah.

943 Rutan, D.A., F.G. Rose, N.M. Smith, T.P. Charlock, 2001: Validation data set for CERES  
 944 surface and atmospheric radiation budget (SARB), WCRP/GEWEX Newsletter, 11,  
 945 No. 1, 11-12.

946 Rutan, D., T. Charlock, F. Rose, S. Kato, S. Zentz, and L. Coleman, 2006: Global  
 947 Surface Albedo from CERES/TERRA Surface and Atmospheric Radiation Budget

948 (SARB) Data Product. Proceedings of 12th Conference on Atmospheric Radiation  
 949 (AMS), 10-14 July 2006, Madison, Wisconsin.

950 Salomon, J.G., A. H. Strahler, F. Gao, Y. Jin, 2006: Validation of the MODIS bi-  
 951 directional reflectance distribution function and albedo retrievals using combined  
 952 observation from the Aqua and Terra platforms. *IEEE Trans. On Geosci., and Rem.*  
 953 *Sens.*, 44, No. 6, 1555-1564.

954 Schaaf, C. B., F. Gao, A. H. Strahler, W. Lucht, X. Li, T. Tsang, N. C. Strugnell, X.  
 955 Zhang, Y. Jin, J. P. Muller, P. Lewis, M. Barnsley, P. Hobson, M. Disney, G.  
 956 Roberts, M. Dunderdale, C. Doll, R. d'Entremont, B. Hu, S. Liang, and J. L. Privette,  
 957 2002: First operational BRDF albedo nadir reflectance products from MODIS.  
 958 *Remote Sens. Environ.*, 83, 135–148.

959 Smith, G. L., and R. N. Green, 1981: Deconvolution of wide field-of-view radiometer  
 960 measurements of earth-emitted radiation. Part I: Theory. *J. Atmos. Sci.*, 38, 461-  
 961 473.

962 Smith, W. L. Jr., T.P. Charlock, R. Kahn, J.V. Martins, L.A. Remer, P.V. Hobbs, J.  
 963 Redemann, C.K. Rutledge, 2005: EOS-TERRA aerosol and radiative flux validation:  
 964 An overview of the Chesapeake Lighthouse and Aircraft Measurements for Satellites  
 965 (CLAMS) experiment. . *J. Atmos. Sci.*, 62, 903-918.

966 Suttles, J. T., R. N. Green, P. Minnis, G. L. Smith, W. F. Staylor, B. A. Wielicki, I. J.  
 967 Walker, D. F. Young, V. R. Taylor, and L. L. Stowe, 1988: Angular radiation models  
 968 for the earth-atmosphere system. Vol. I: Shortwave Radiation. NASA Ref. Publ.  
 969 RP-1184, 147 pp.

Tegen, I., and A. A. Lacis, 1996: Modeling of particle size distribution and its influence  
 on the radiative properties of mineral dust aerosol. *J. Geophys. Res.*, 101, 19,237-  
 19,244.

Wang, Z., X. Zeng, and M. Barlage, 2007: Moderate resolution imaging  
 spectroradiometer bidirectional reflectance distribution function-based albedo  
 parameterization for weather and climate models. *J. Geophys. Res.*, 112, D02103,  
 doi:10.1029/2005JD006736.

Wielicki, B. A., B. R. Barkstrom, E. F. Harrison, R. B. Lee III, G. L. Smith, and J. E.  
 Cooper, 1996: Clouds and the Earth's Radiant Energy System (CERES): An Earth  
 Observing System Experiment, *Bull. Amer. Meteor. Soc.*, 77, 853-868.

Yang, S.-K., S. Zhou, and A. J. Miller, 2000: SMOBA: A 3-D daily ozone analysis  
 using SBUV/2 and TOVS measurements.  
[www.cpc.ncep.gov/products/stratosphere/SMOBA/smoba\\_doc.shtml](http://www.cpc.ncep.gov/products/stratosphere/SMOBA/smoba_doc.shtml)

Zhou, Y., K. C. Rutledge, T. P. Charlock, N. C. Loeb, S. Kato, 2001: Atmospheric  
 correction using MODTRAN for TOA and surface BRDF characteristics from high  
 resolution spectroradiometric/angular measurements from helicopter platform,  
*Advances in Atmos. Sci.* 18, 984-1004.

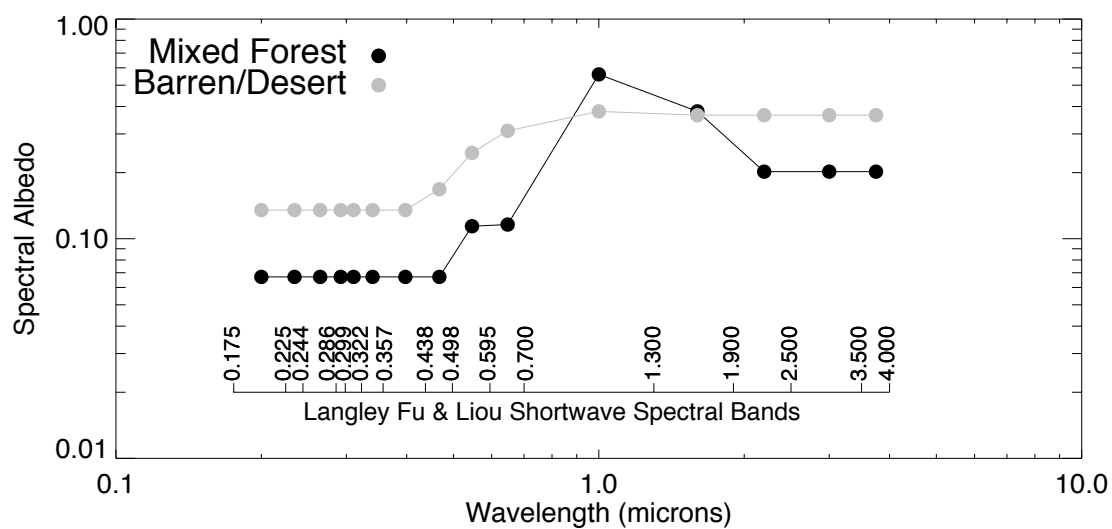


Figure 1. Shortwave spectral bands used in Langley Fu & Liou 2005 (LFL05) radiation transfer model, and spectral albedo associated in Clouds & Radiation Swath processing for IGBP scene types Mixed Forest and Barren Desert.

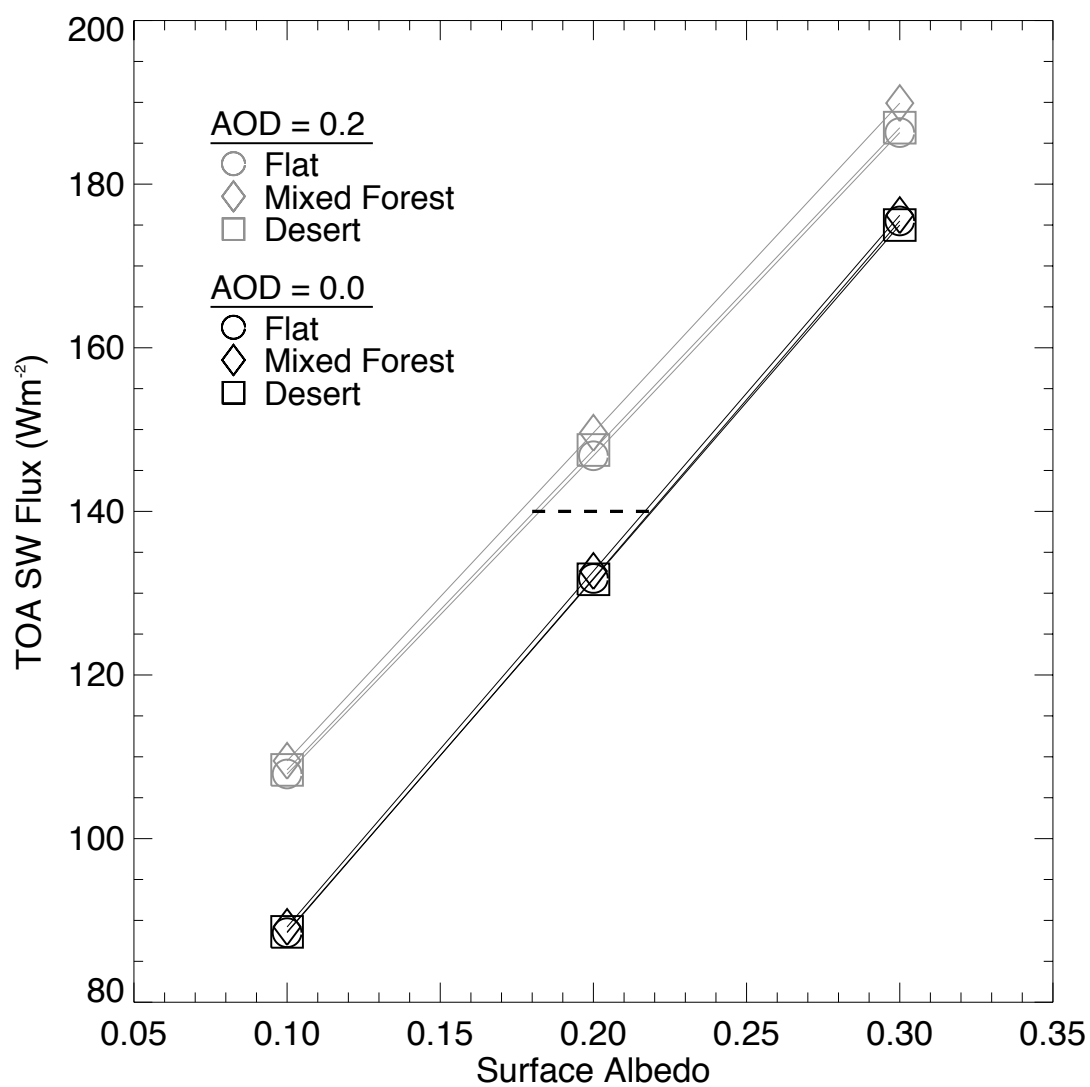


Figure 2. Change in TOA SW Flux with change in spectral surface albedo and aerosol optical depth.

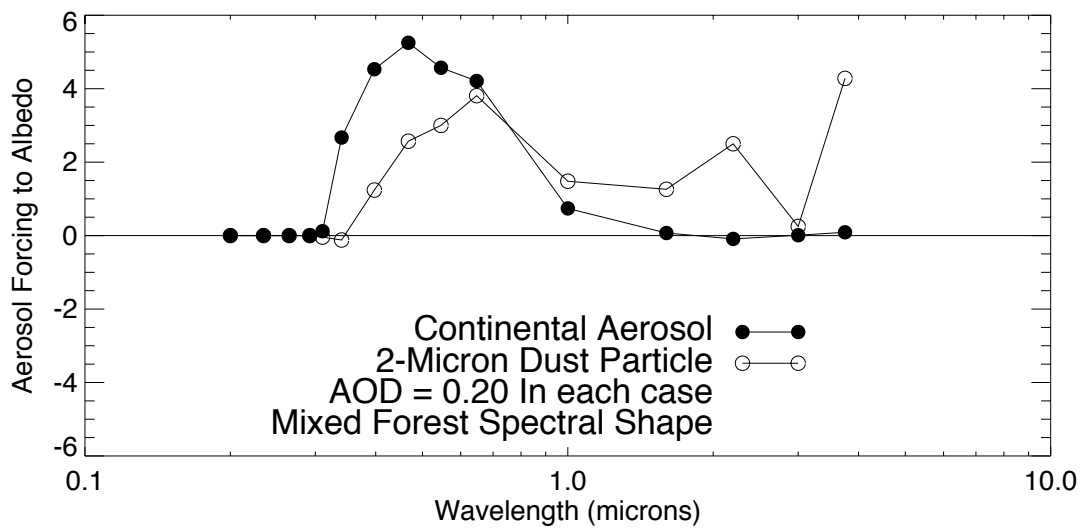


Figure 3. Spectral forcing of TOA Albedo due to two different aerosol types.

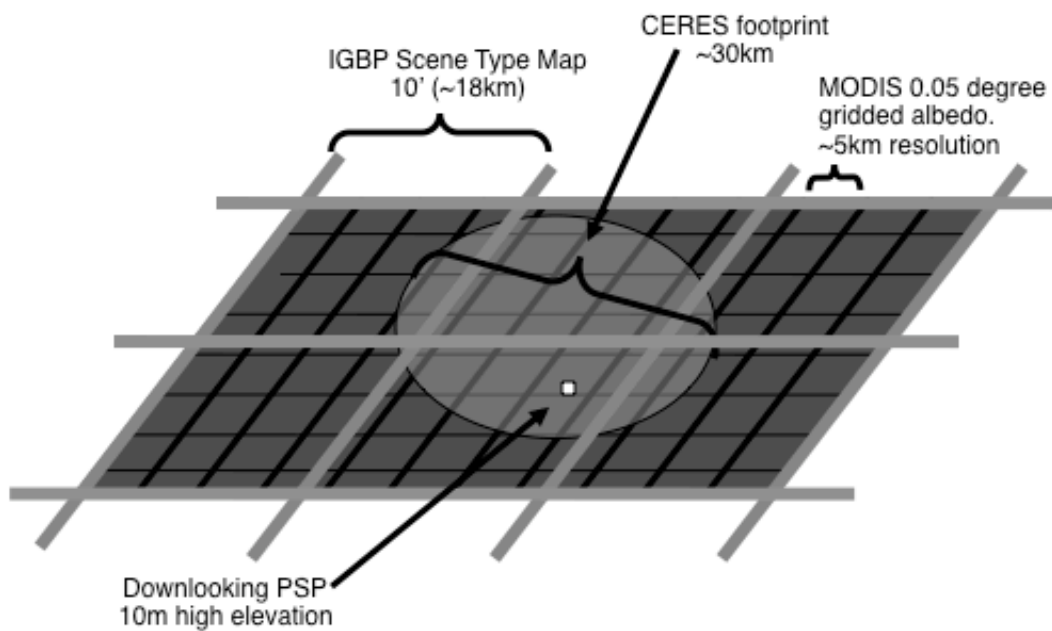


Figure 4. Cartoon showing CERES footprint MODIS grid and IGBP grid relative to one-another.



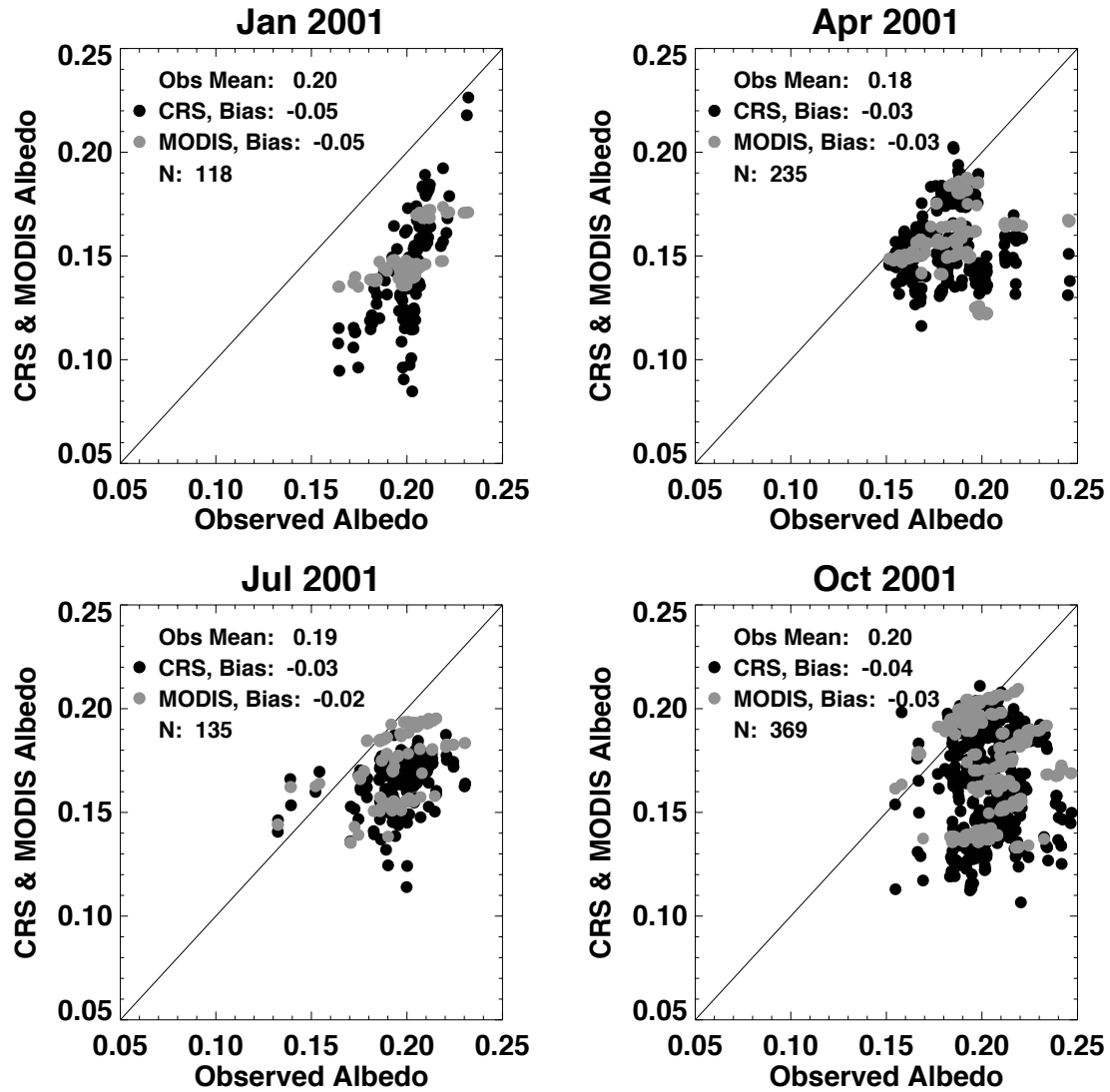


Figure 5. CERES CRS and MODIS 5km MCD32C2 albedo compared to observed surface albedos at 14 land surface sites where surface albedo is observed during four months in 2001.

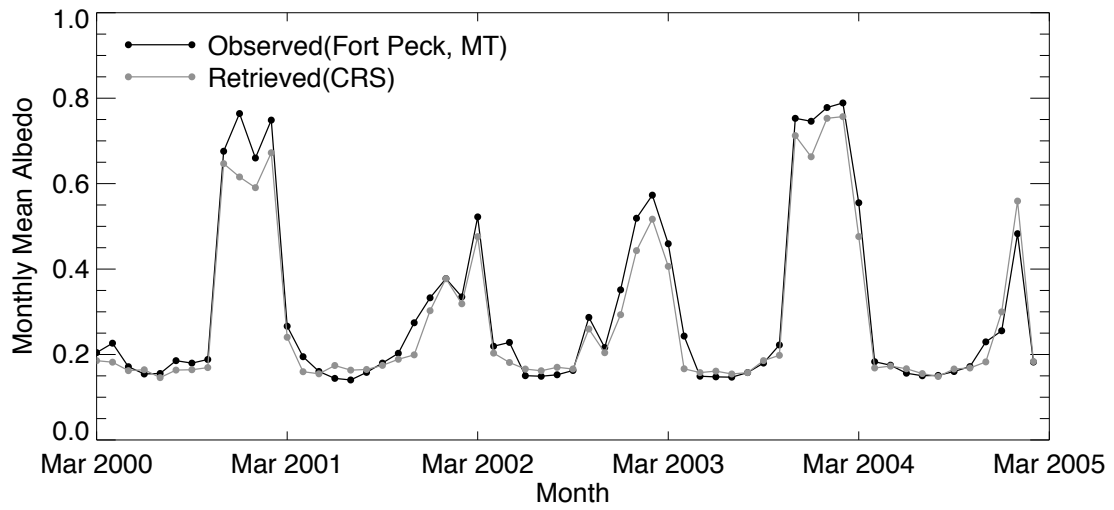


Figure 6. Time series of observed (black) and retrieved (gray) albedo near Fort Peck, MT.

Values represent a mean for the month at the of CERES observations.

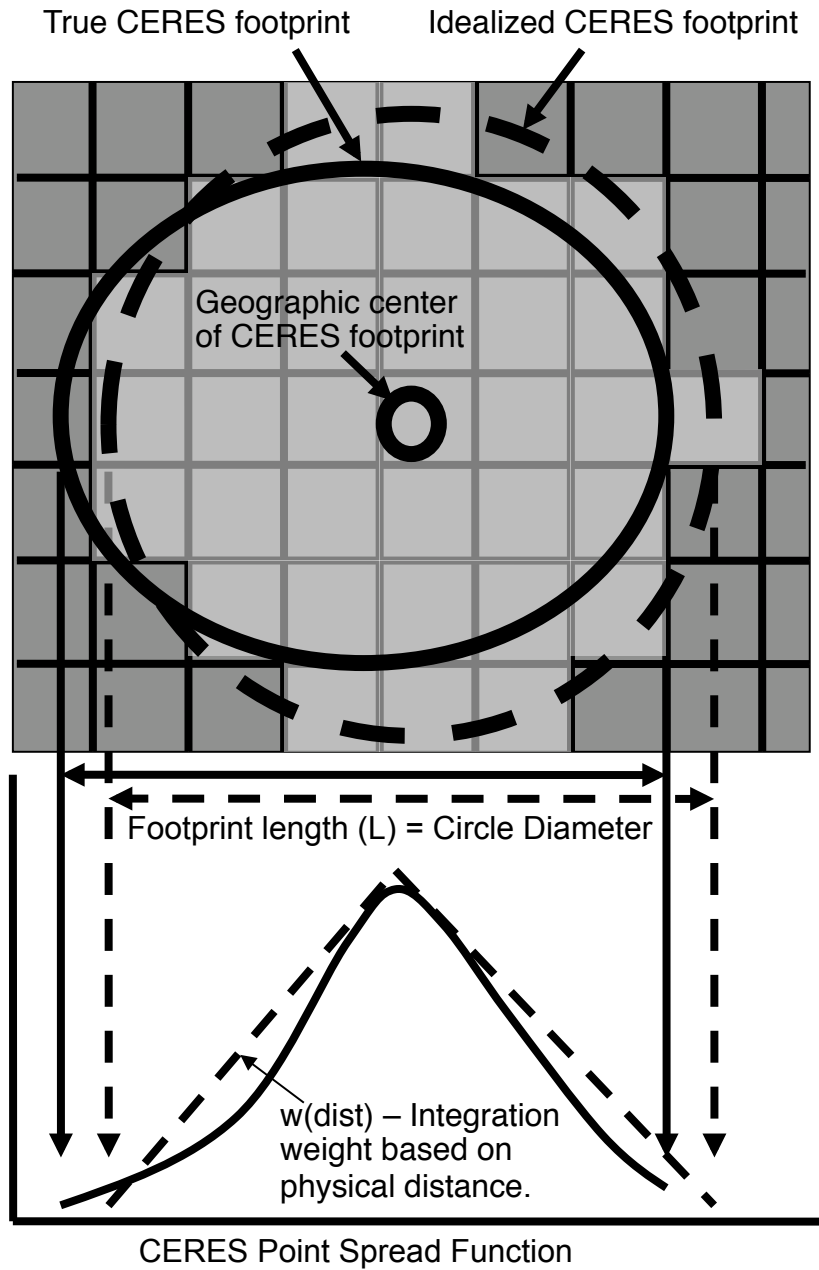


Figure 7. Schematic of placement of MODIS gridded ‘pixels’ inside of larger CERES footprint and integration weights.

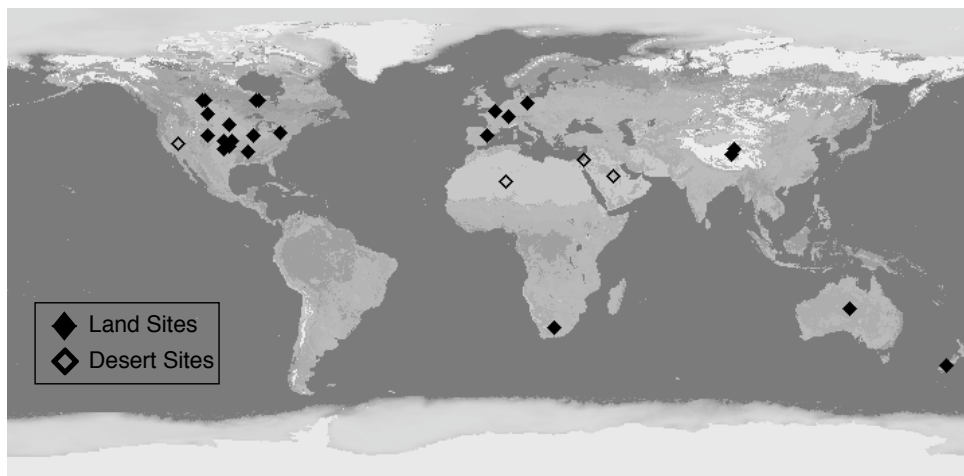


Figure 8. Map showing locations on the globe where the CERES and MODIS albedos are collocated for comparison. Sites are divided into 25 land and 4 desert locations.

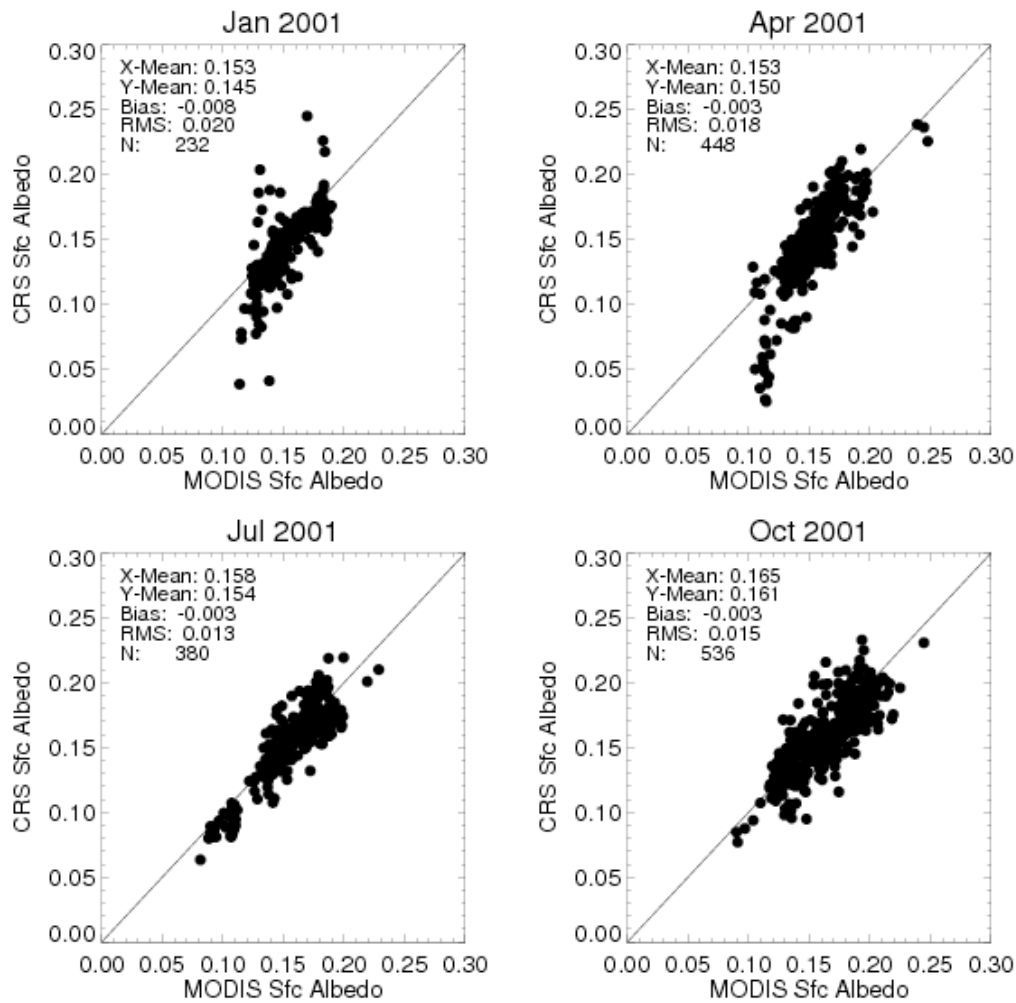


Figure 9. Comparison of CRS surface albedo to MODIS albedo integrated within coincident CERES footprints.

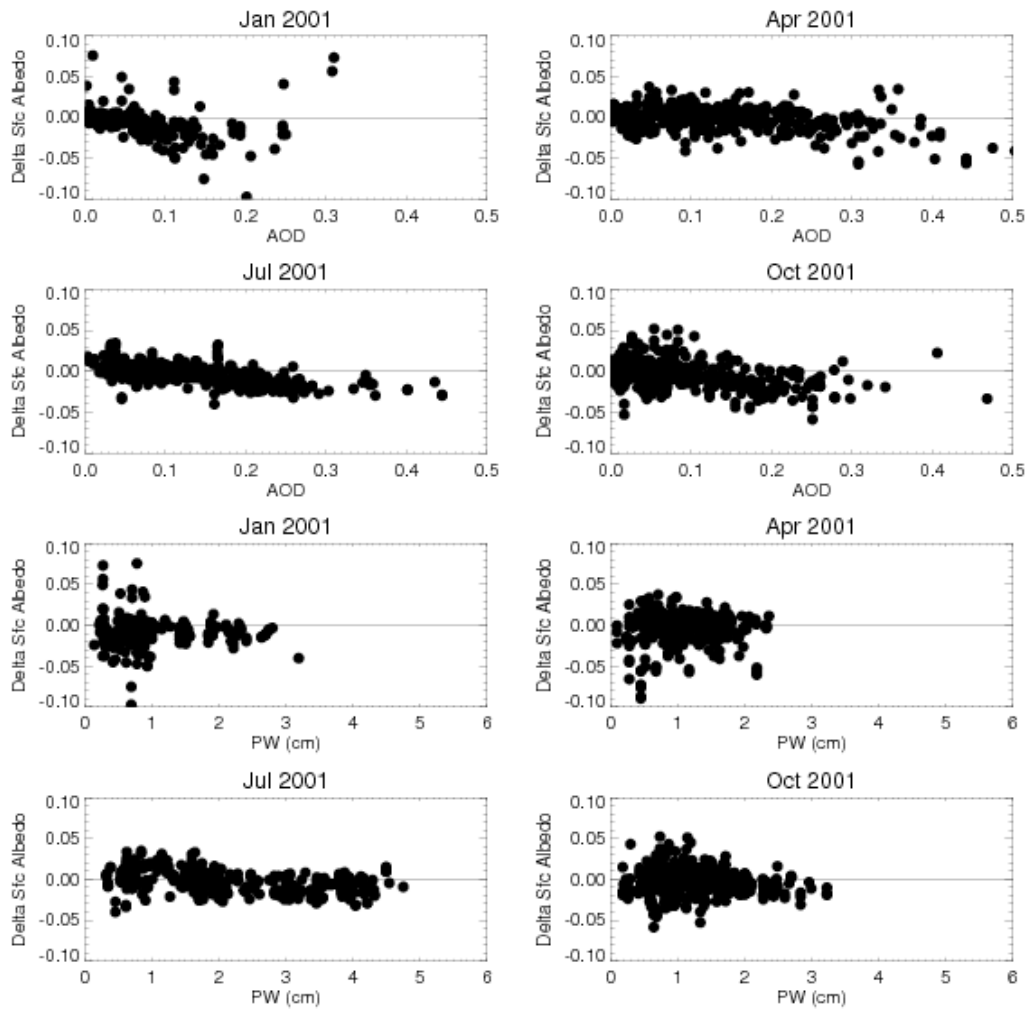


Figure 10. Difference in CRS and MODIS albedos for each month as a function of aerosol optical depth and precipitable water used in CRS calculations.

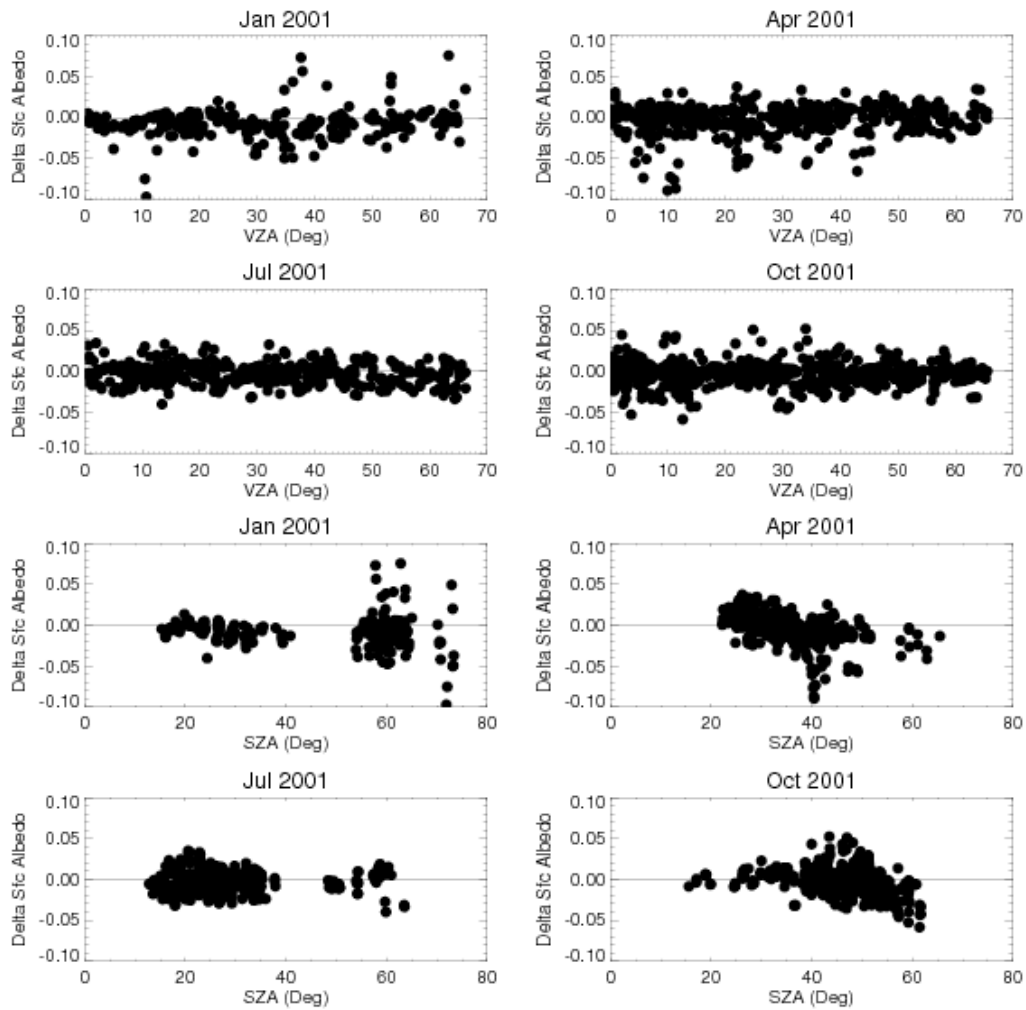


Figure 11. Difference in CRS and MODIS albedo for “land” validation sites for all four months as a function of viewing zenith (VZA) and solar zenith (SZA) angle at time of CERES observation.

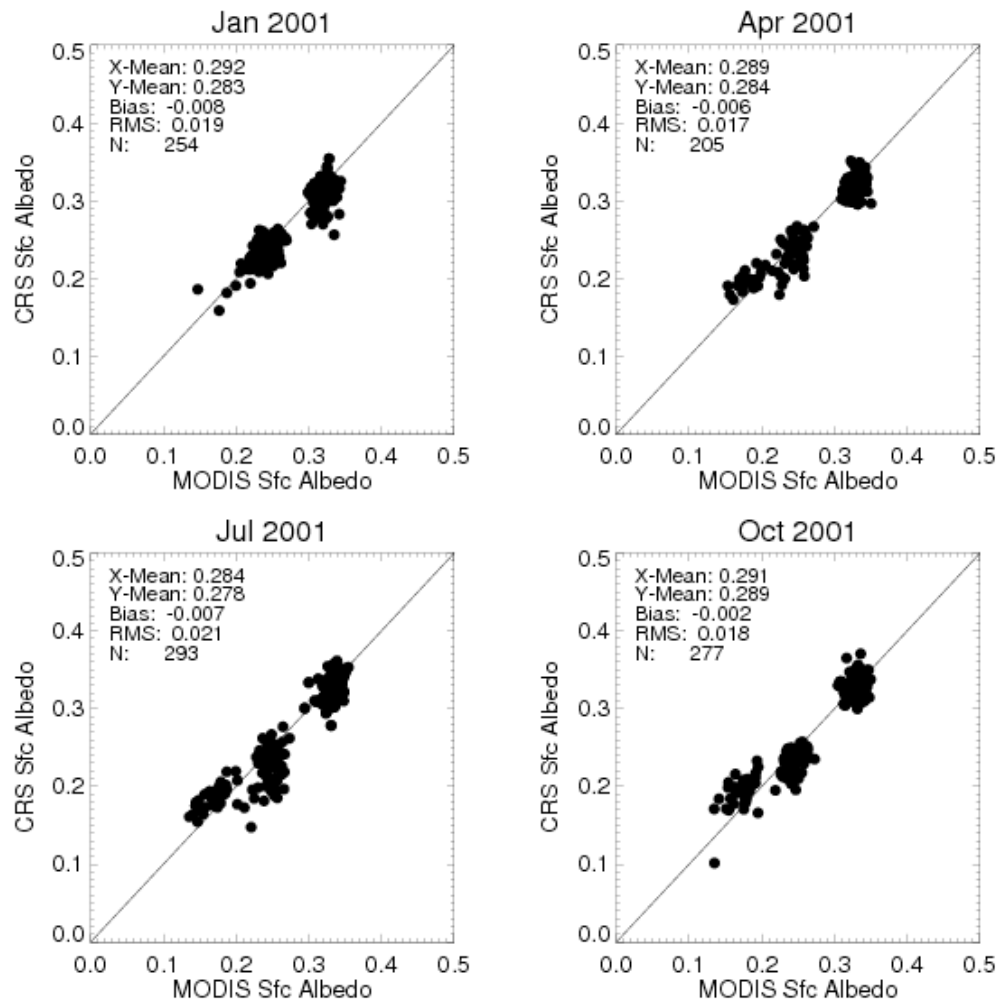


Figure 12. Comparison of CRS and MODIS albedo at four desert locations around the globe.



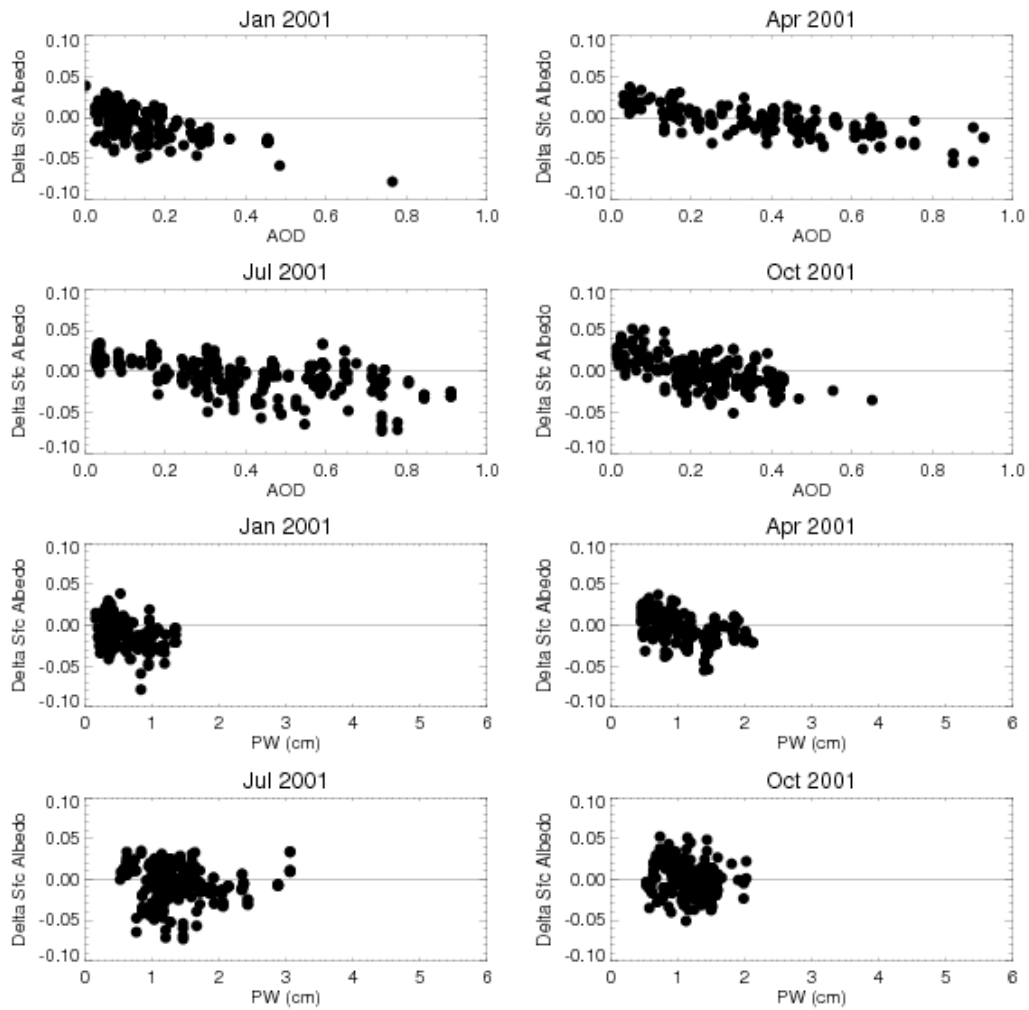


Figure 13. Difference between CRS and MODIS albedo at desert locations as a function of aerosol optical depth and precipitable water.

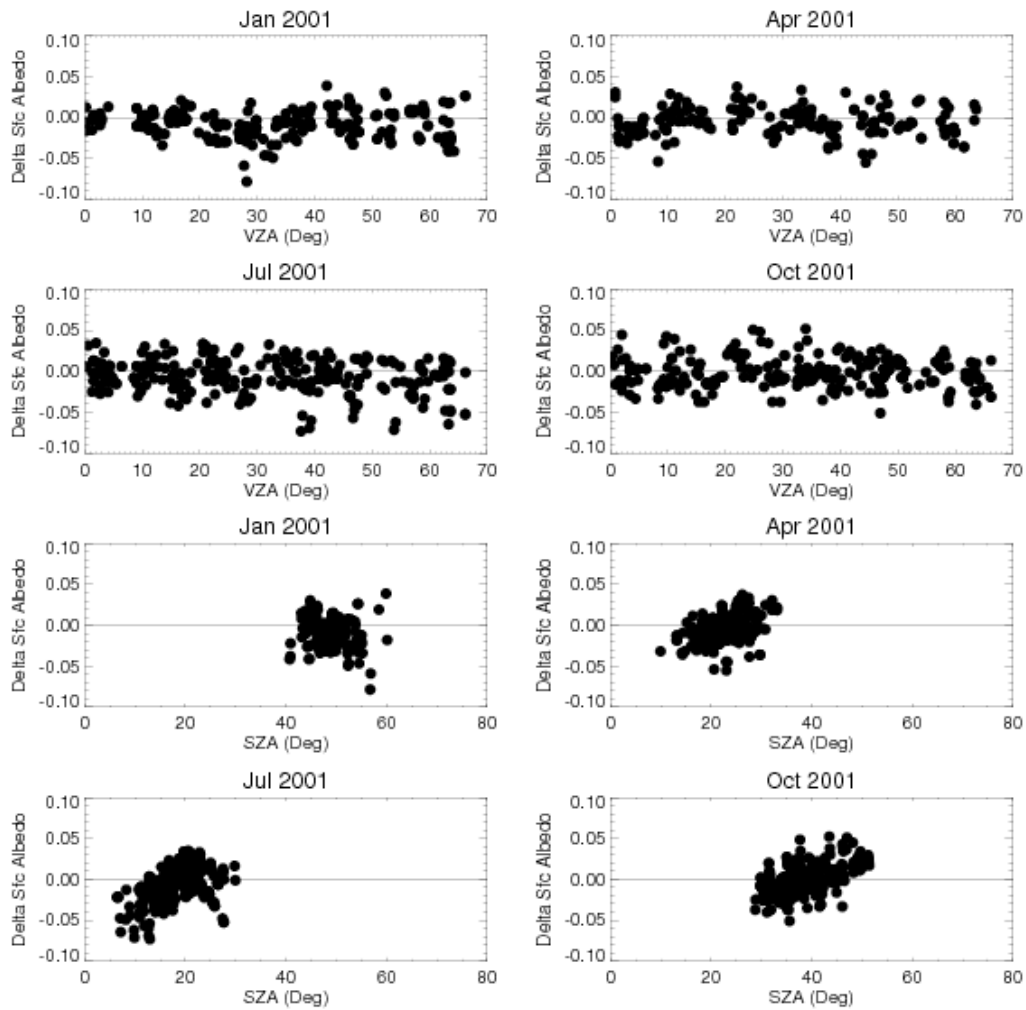


Figure 14. Difference in CRS and MODIS albedo for “desert” validation sites for all four months as a function of viewing zenith (VZA) and solar zenith (SZA) angle at time of CERES observation.

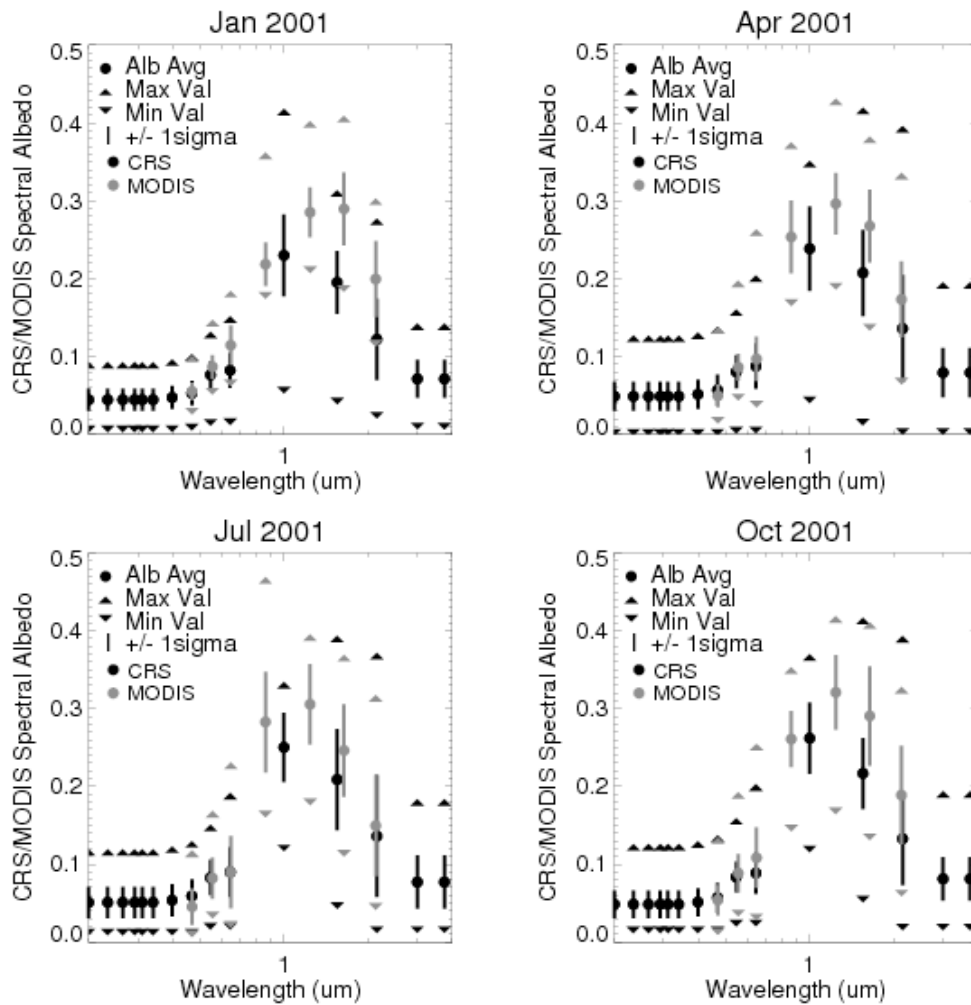


Figure 15. Land surface spectral albedos for CRS (in 15 Langley Fu & Liou bands) and 7 MODIS channels shown as a mean, maximum, minimum and 1 standard deviation for all comparison points.

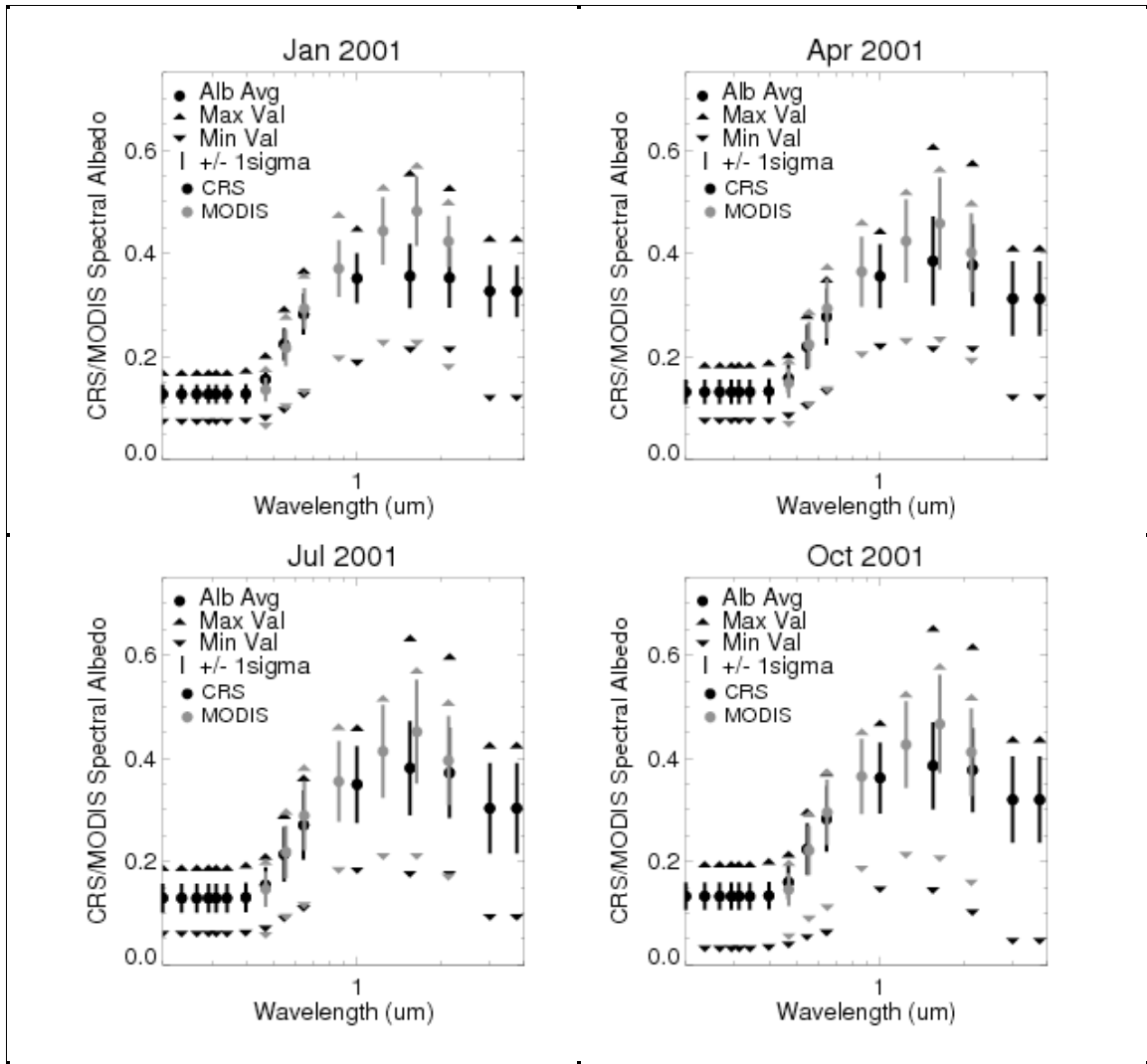


Figure 16. Desert surface spectral albedos for CRS (in 15 Langley Fu & Liou bands) and 7 MODIS channels shown as a mean, maximum, minimum and 1 standard deviation for all comparison points.

1117

1118